

# Blasts from the Past: Supernova Shock Breakouts among X-Ray Transients in the *XMM-Newton* Archive

DENNIS ALP <sup>1</sup> AND JOSEFIN LARSSON <sup>1</sup>

<sup>1</sup>*Department of Physics, KTH Royal Institute of Technology, and The Oskar Klein Centre, SE-10691 Stockholm, Sweden*

(Received April 20, 2020; Revised May 7, 2020; Accepted May 7, 2020)

Submitted to ApJ

## ABSTRACT

The first electromagnetic signal from a supernova (SN) is released when the shock crosses the progenitor surface. This shock breakout (SBO) emission provides constraints on progenitor and explosion properties. Observationally, SBOs appear as minute to hour-long extragalactic X-ray transients. They are challenging to detect and only one SBO has been observed to date. Here, we search the *XMM-Newton* archive and find twelve new SN SBO candidates. We identify host galaxies to nine of these at estimated redshifts of 0.1–1. The SBO candidates have energies of  $\sim 10^{46}$  erg, timescales of 30–3000 s, and temperatures of 0.1–1 keV. They are all consistent with being SN SBOs, but some may be misidentified Galactic foreground sources or other extragalactic objects. SBOs from blue supergiants agree well with most of the candidates. However, a few could be SBOs from Wolf–Rayet stars surrounded by dense circumstellar media, whereas two are more naturally explained as SBOs from red supergiants. The observations tentatively support non-spherical SBOs and are in agreement with asymmetries predicted by recent three-dimensional SN explosion simulations. *eROSITA* may detect  $\sim 2$  SBOs per year, which could be detected in live analyses and promptly followed up.

**Keywords:** Core-collapse supernovae (304); X-ray transient sources (1852); Massive stars (732); Shocks (2086)

## 1. INTRODUCTION

The shock breakout (SBO) emission is the first electromagnetic signal from a supernova (SN; Waxman & Katz 2017; Levinson & Nakar 2019). This emission carries information about the structure of the progenitor star. The most important physical properties that can be constrained are the progenitor radius, asymmetries, and final mass-loss history. This means that SBOs offer a unique avenue to probe SN progenitors (Smartt 2009) and the SN explosion mechanism (Janka et al. 2016).

The SBO emission is released when the radiation mediated shock from the SN explosion crosses the surface of the star. However, if the circumstellar medium (CSM) is sufficiently dense, the shock can propagate into the CSM and result in a longer “CSM breakout”. SBOs from the progenitor surface typically peak in X-rays, and evolve into ultraviolet and optical as the envelope cools and the ejecta expand. Extended CSM breakouts and the post-breakout cooling phase evolve on timescales of  $> 1$  day and are easier to detect. These timescales are within the reach of recent wide-field optical SN surveys (Waxman &

Katz 2017 and references therein). Henceforth, we focus on X-ray SBOs that evolve on timescales much shorter than 1 day. The initial SBO and post-breakout cooling phase precede the commonly observed, months-long SN emission that is powered by reprocessed radioactive decay.

The observable properties of SN SBOs are expected to be different for different progenitor types. Typical SBO energies, timescales, and temperatures (Matzner & McKee 1999; Nakar & Sari 2010; Sapir et al. 2013) for red supergiants (RSGs) are  $10^{48}$  erg, 1000 s, and 0.03 keV, respectively. The corresponding values are  $10^{46.5}$  erg, 100 s, and 0.3 keV for blue supergiants (BSGs); and  $10^{45}$  erg, 10 s, and 3 keV for Wolf–Rayet (WR) stars. This assumes spherical symmetry, as well as negligible effects of the CSM. SBOs from RSGs are very soft and are expected to be heavily absorbed by the interstellar medium (ISM). In contrast, WR SBOs are much harder, but the total number of emitted photons is several orders of magnitude lower. Both the increased temperature (higher photon energies) and lower total energy reduce

the total number of emitted photons, which makes WR SBOs difficult to detect. BSGs are the progenitor type that is most likely to be detected due to the trade-off between peak energy and number of emitted photons (Calzavara & Matzner 2004; Sapir et al. 2013; Waxman & Katz 2017). Finally, we note that thermonuclear SNe are expected to produce SBOs with temperatures of  $\sim 20$  keV. These SBOs are not expected to be detectable because the timescales are approximately 10 ms and the total energies are on the order of  $10^{40}$  erg (Piro et al. 2010; Nakar & Sari 2010).

Theoretical aspects of SBOs have been studied for several decades. Early works explored the emission from non-relativistic SBOs with simplified physics and for specific progenitor structures (e.g. Weaver 1976; Klein & Chevalier 1978; Ensman & Burrows 1992). More recent works have focused on developing models for more realistic progenitor structures with more detailed treatments of the relevant physics (Katz et al. 2010; Nakar & Sari 2010; Sapir et al. 2011; Katz et al. 2012; Sapir et al. 2013; Ito et al. 2020). Notably, several theoretical works have stressed that many SBOs should have been serendipitously observed by previous and existing X-ray telescopes (Klein & Chevalier 1978; Calzavara & Matzner 2004; Sapir et al. 2013; Sapir & Halbertal 2014; Waxman & Katz 2017). The telescopes most likely to have detected SBOs are *XMM-Newton*, which has been in service since 2000, followed by *ROSAT*, which collected data between 1990 and 1999.

Despite the significant theoretical efforts, few observational searches have been performed, and only the SBO from SN 2008D has been detected (Soderberg et al. 2008). The SBO detection from SN 2008D was serendipitously detected as a bright X-ray transient in a scheduled *Swift* observation of NGC 2770. In addition to the direct detection of SN 2008D, the SBO from SN 1987A was indirectly observed by the effects of the SBO on the CSM (Ensmann & Burrows 1992; Blinnikov et al. 2000). The only systematic searches in archival X-ray data for transients with SBO-like properties were of the *ROSAT* archive (Vikhlinin 1998; Greiner et al. 2000). Interestingly, Vikhlinin (1998) reported a number of candidates but was unable to securely identify their origins. While no systematic searches for SBOs have been carried out recently, transients on longer timescales have been studied, primarily in the *Chandra* archive (Bauer et al. 2017; Xue et al. 2019; Yang et al. 2019).

In this paper, we search for SN SBOs in archival *XMM-Newton* data. Observationally, this implies that we search all public *XMM-Newton* observations for X-ray transients on timescales shorter than approximately 10 ks. To our knowledge, the *XMM-Newton* data

have not been systematically searched for this kind of transient, even though several SBOs are predicted to be present in the data. We aim to identify SBO candidates and investigate the implications for the SN progenitors.

This paper is organized as follows. We describe the SBO search and identification process in Section 2, the host galaxies in Section 3, and provide details related to the data reduction of the final candidates in Section 4. The spectral fitting is described in Section 5 and observed properties of the SBOs are presented in Section 6. We investigate the SBO interpretation and its implications in Section 7, discuss contaminants and other potential astrophysical sources in Section 8, and conclude in Section 9.

All uncertainties are  $1\sigma$  and one-sided limits are  $3\sigma$  unless stated otherwise. We adopt a flat  $\Lambda$ CDM cosmology with a Hubble–Lemaître constant  $H_0 = 70 \text{ km s}^{-1} \text{ Mpc}^{-1}$  and  $\Omega_\Lambda = 0.73$ .

## 2. IDENTIFYING SBO CANDIDATES

To find SN SBO candidates, we search for X-ray transients with typical timescales shorter than  $\sim 10$  ks in archival *XMM-Newton* data. These X-ray transients can only be observed if they happen to occur within the field of view (FoV) of an X-ray telescope because SBOs decay well before the optical signal from a SN is detected (typically days or weeks later). *XMM-Newton* (Jansen et al. 2001) is the telescope that is most likely to serendipitously observe SBOs because of the combination of its high effective area, high angular resolution, and large FoV of  $\sim 0.2 \text{ deg}^2$ . For theoretically predicted BSG SBO properties (Section 1), we expect our search to be sensitive to a redshift of  $\sim 1$ . This assumes favorable observing conditions and a low level of absorption along the line of sight.

Before performing a blind search for X-ray transients, we crossmatch all *XMM-Newton* observations with known SNe and gamma-ray bursts (GRBs). In the current context, we restrict the matches to X-ray detections of the SBO, long before the optical SN detection or simultaneous with the prompt GRB phase. The purpose is to check if any known SNe or GRBs have been serendipitously observed, but we find none. The catalog of SNe is from the Latest Supernovae website<sup>1</sup> and the GRBs are from the *Swift*/BAT GRB Catalog (Lien et al. 2016). The SN catalog covers the entire *XMM-Newton* lifetime, while the GRB data is limited to the lifetime of *Swift* because only GRBs with sufficiently accurate positions can be crossmatched.

<sup>1</sup> Previously known as “Bright Supernovae”: <http://www.rochesterastronomy.org/snimages/sndateall.html>

### 2.1. Finding Transients

To avoid detecting a large number of variable Galactic X-ray sources unrelated to SN SBOs, we immediately reject all sources that are close to a star in Gaia or a known Galactic source in SIMBAD. More precisely, we reject sources within 5 arcsec of an object in Gaia DR2 (Gaia Collaboration et al. 2018) with a (positive) parallax with a significance greater than  $3\sigma$ . Similarly for SIMBAD, we reject X-ray sources if there is a SIMBAD object within 5 arcsec classified as a star, white dwarf, neutron star, black hole, or combinations thereof (i.e. binaries).

We develop a custom transient finder algorithm that we apply to all observations, and also search for transients among the sources in the 3XMM-DR8 catalog (Rosen et al. 2016). The details of both search methods are provided in Appendix A. The custom search algorithm is the most general and detects any transients starting from the event lists. The 3XMM-DR8 search focuses on identifying transient behavior among the cataloged X-ray sources. The two algorithms are largely redundant, but are complementary in some respects. The main difference is that our custom search is performed on all public observations with data archived at HEASARC as of 2019 November 11, whereas the latest observation included in 3XMM-DR8 is from 2017 November 30. We note that the standard proprietary period is 1 year after data delivery, which means that the availability of public data during the last 12–14 months of the time intervals is sparse. Our custom algorithm is very simple and does not treat the background and instrumental effects as carefully as 3XMM-DR8.

The two algorithms identify  $\sim 11,000$  transient sources and we manually inspect the light curves, the time-integrated X-ray spectra, and images of these objects. The spectra and images are primarily useful for recognizing instrumental artifacts, variability caused by problematic extraction regions, and blended sources. Instrumental artifacts are generally restricted to one of the cameras and often affect individual pixels or columns. This is very different from astrophysical sources, which are convolved by the point spread function (PSF) of the telescope in all cameras. The screening process up to this point reduces the number of X-ray transients to around 600.

### 2.2. Source Classification

The final step is to separate the extragalactic transients from Galactic foreground sources and artifacts. This separation essentially finds all SBO candidates since SBOs are required to be associated with galaxies. The remaining non-SBO transients are primarily flar-

ing dwarf stars that lack parallax in Gaia and are not identified in SIMBAD, or instrumental artifacts that are difficult to identify in time-integrated images. To perform this final selection, we use time-resolved spectra and images. Additionally, we search all catalogs available at VizieR (Ochsenbein et al. 2000) and inspect available sky images of the source position (primarily X-rays, optical, and near-infrared; NIR). We primarily use all HiPS sky images available through CDS/Aladin (Bonnarel et al. 2000; Boch & Fernique 2014), but also check for data in MAST, ESO Portal, and HEASARC in some cases. All objects that show clear signs of being instrumental, Galactic, or persistent are discarded.

We separate stars from galaxies using the optical and NIR images. The primary data used for host classification are from Pan-STARRS (Chambers et al. 2016), DES (Abbott et al. 2018), and SkyMapper (Wolf et al. 2018). We use morphological classifiers to identify extended sources (galaxies)<sup>2</sup>, as well as stellarity catalogs (McMahon et al. 2013; Tachibana & Miller 2018). However, since we are interested in accurate classifiers of a few objects, we largely rely on visual inspection of available data for each object. The manual classification of sources generally agrees with automatic and objective classifiers, but allows us to identify rare cases, such as likely misclassifications due to blending of neighboring stars.

All objects that are possible SN SBOs are added to the final sample. This decision is based on the light curve shape, duration, spectral shape, and the probability that the source is extragalactic based on available information. Furthermore, we require that the initial rise and a substantial part of the decay is contained within the observation. We discard sources that show persistent emission that appears associated with the transient before the initial rise, which would indicate that the source is a flaring persistent source. We do not discard any transients because they are too short. This means that the lower limit is effectively set by the temporal resolution of *XMM-Newton*, which is on the order of 100 ms for the most common observing modes. We also do not discard any transients because they are too long, but they are indirectly limited by the requirement of rising and decaying within the exposure time (typically 10–130 ks). We do not use quantitative requirements at this last stage because of the difficulty of strictly defining the acceptable properties.

<sup>2</sup> e.g. <https://outerspace.stsci.edu/display/PANSTARRS/How+to+separate+stars+and+galaxies>

**Table 1.** Identifiers of SBO Candidates

XT	$\alpha$	$\delta$	$l$	$b$	$\sigma$	Obs. ID	Time
	( $^{\circ}$ )	( $^{\circ}$ )	( $^{\circ}$ )	( $^{\circ}$ )	( $''$ )		YYYY Mmm dd hh:mm:ss
161028	263.23663	43.51250	69.22769	32.05326	1.6	0781890401	2016 Oct 28 02:39:35
151219	173.53096	0.87354	264.47274	57.85230	1.6	0770380401	2015 Dec 19 03:13:20
110621	37.89595	-60.62934	283.01881	-52.45370	1.8	0675010401	2011 Jun 21 18:43:20
030206	29.28818	37.62732	137.06247	-23.43464	1.3	0149780101	2003 Feb 06 03:52:30
070618	24.27520	-12.95280	162.18014	-72.24921	1.4	0502020101	2007 Jun 18 21:03:55
060207	196.83165	-40.46064	306.19786	22.31033	1.8	0300240501	2006 Feb 07 18:16:20
100424	321.79670	-12.03906	40.02322	-39.95127	1.7	0604740101	2010 Apr 24 18:30:00
151128	167.07789	-5.07517	261.31731	49.28100	2.0	0760380201	2015 Nov 28 23:20:00
050925	311.43725	-67.64702	327.21796	-35.70622	2.0	0300930301	2005 Sep 25 02:53:20
160220	204.19991	-41.33736	312.01496	20.73297	1.6	0765041301	2016 Feb 20 07:28:20
140811	43.65356	41.07430	146.61178	-16.06542	1.5	0743650701	2014 Aug 11 19:36:40
040610	169.53625	7.70266	249.93237	60.57574	1.5	0203560201	2004 Jun 11 01:53:20

NOTE—Candidates are listed in descending order of confidence of being a SN SBO. The same ordering is used throughout the paper. The last four candidates may be misidentified Galactic foreground sources (Section 8.1). We provide celestial coordinates in both the equatorial ( $\alpha$ ,  $\delta$ ) and Galactic ( $l$ ,  $b$ ) systems. The parameter  $\sigma$  refers to the astrometric uncertainty and the last column provides the start times of the transients in UTC.

We verify completeness of the search by inspecting the 100,000 most variable light curves from 3XMM-DR8 by eye to look for transients that were potentially missed by the algorithms, and find one additional faint candidate. The level of variability in this context is measured by a likelihood test under the assumption that the light curve bin uncertainties are Gaussian. Altogether, we find 12 SN SBO candidates. Identifiers of the SN SBO candidates are provided in Table 1. We designate each candidate by “XT” followed by the date; the first two numbers correspond to the year, the second two numbers to the month, and the last two numbers to the day (analogous to GRBs). We choose to present the SBO candidates in descending order of confidence (loosely defined) throughout this paper.

### 3. HOST GALAXIES

Table 2 provides key parameters for the host galaxy candidates associated with the 12 transients. For reference, we also provide optical and NIR photometry of the hosts when available, and limits otherwise, in Table B.1. Three of the transients have no clearly identified host, and it is also possible that some of the observed hosts are Galactic objects misclassified as galaxies. We discuss potential misidentifications and alternative sources for the X-ray transients in Section 8. Throughout the rest of the paper, we assume that the X-ray transients are SN SBOs.

The most important parameter for the inferred properties of the transients is the redshift ( $z$ ). Some of the redshifts are highly uncertain and we stress that this uncertainty propagates into parameters that depend on  $z$ . This mainly applies to the discussion of inferred SN properties in Section 7.2. In contrast, the observed properties in Section 6 are largely independent of  $z$ , with the only effect being an energy shift of the fitted temperature and host galaxy absorption. The magnitude of this effect is relatively small ( $\propto 1 + z$ ) and does not qualitatively alter the results.

To estimate the redshifts of the host galaxies, we primarily rely on SED template fitting. Photometric redshift techniques are generally more reliable if the Balmer (4000 Å) or Lyman (912 Å) break falls between two broad filters. This means that the optical data (Table B.1) is the most constraining for our sources. Furthermore, we only use data from one survey (for each object) to ensure that the photometry is homogeneous in the sense that colors are correctly represented. For these reasons, we exclude the NIR data from the SED fitting procedure. We are able to perform SED fits to seven hosts, whereas the remaining five either lacked an identified host or multi-band optical data.

In addition to the SED fitting, we also consider additional independent information. The second most important constraint on  $z$  comes from the redshifts of neighboring galaxies. We utilize this when the SED fit



**Table 2.** Host Candidates

XT	$\alpha$	$\delta$	Offset	$P_{\text{gal}}$	$z$	$\mu$	Scale	$M_r$	Galaxy
	( $^{\circ}$ )	( $^{\circ}$ )	( $''$ )			(mag <sub>AB</sub> )	(kpc arcsec <sup>-1</sup> )	(mag <sub>AB</sub> )	
161028	263.23707	43.51231	1.3	1.00	0.29	40.9	4.4	−20.2	SB
151219	173.53037	0.87409	2.9	0.99	0.62	42.9	6.9	−21.4	Sbc
110621	37.89582	−60.62918	0.6	0.99	0.095	38.2	1.8	−18.6	SB
030206	29.28776	37.62768	1.8	...	1.17	44.6	8.4	−22.5	SB
070618	...	...	...	...	0.37	41.5	5.2	> −17.4	...
060207	...	...	...	...	0.3 <sup>a</sup>	41.0	4.5	> −19.9 <sup>b</sup>	...
100424	321.79659	−12.03900	0.5	1.00	0.13	38.9	2.3	−18.6	Sa
151128	167.07885	−5.07495	3.5	1.00	0.48	42.2	6.0	−21.9	Sd
050925	311.43769	−67.64740	1.5	0.99	0.3 <sup>a</sup>	41.0	4.5	−20.3 <sup>b</sup>	...
160220	204.19926	−41.33718	1.9	0.90	0.3 <sup>a</sup>	41.0	4.5	−20.7 <sup>b</sup>	...
140811	43.65365	41.07406	0.9	0.75	0.57	42.6	6.6	−22.0	Sb
040610	...	...	...	...	0.50	42.3	6.2	> −19.5	...

NOTE—Offset is the distance between the transient and the host galaxy. We note that the offsets are comparable to the uncertainties of the X-ray positions (Table 1).  $P_{\text{gal}}$  is the probability of the source being a galaxy based on morphology. These values are either from PS1-PSC (Pan-STARRS data, [Tachibana & Miller 2018](#)) or VHS (VISTA data, [McMahon et al. 2013](#)). For convenience, we also provide the distance expressed as the distance modulus ( $\mu$ ), the angular scale, and the absolute magnitude ( $M$ ; in  $r$ -band unless otherwise noted). The “Galaxy” column provides tentative galaxy classifiers based on the SED fitting; Sa, Sb, Sd, and Sbc are late-type spirals, whereas SB denotes starburst galaxies.

<sup>a</sup>Fiducial redshifts of 0.3 are used when insufficient information is available for a redshift estimate.

<sup>b</sup>These values are in the  $J$ -band because the  $r$ -band data is much shallower for these sources.

ting appears unreliable or if optical data of the host is unavailable. After performing the SED fits and potentially including data from neighbors, we check if the favored redshift implies a reasonable absolute magnitude and radius for the galaxy ([Shen et al. 2003](#); [Blanton et al. 2003](#); [Wolf et al. 2003](#); [Ilbert et al. 2005](#)). We also compare the distances with a reconstruction of the large-scale structure ([Lavaux et al. 2019](#), E. Tsaprazi 2020, private communication). The reconstruction of the large-scale structure in the local universe (out to  $z = \sim 0.1$ –1 depending on the line of sight) provides a measure of density as a function of redshift along the line of sight. This is effectively the likelihood of  $z$  relative to the large-scale structure. The inclusion of independent constraints means that we do not always choose the SED fit with the lowest  $\chi^2$  value, but rather analyze all data and adopt the redshift that appears to be most consistent overall. Finally, we note that the information from neighboring galaxies allows us to estimate redshifts even if no host galaxy is directly observed. This is only possible in some cases and is clearly highly uncertain.

We use the **Le PHARE** code ([Arnouts et al. 1999](#); [Ilbert et al. 2006](#)) to perform the SED fitting. The package in-

cludes a number of different galaxy SED libraries. We try to fit all sources using the CWW-Kinney, AVEROIN, CFHTLS, and COSMOS sets. Each set is fitted independently to explore the systematic error introduced by choosing different SED libraries. This also allows us to choose the SED that is most consistent with the supplementary information. The CWW library ([Coleman et al. 1980](#)) is based on four observed spectra (Ell, Sbc, Scd, Irr) and is commonly used for photometric redshift estimates. The CWW-Kinney sample extends the CWW set with six starburst galaxies ([Calzetti et al. 1994](#); [Kinney et al. 1996](#)). Both the AVEROIN ([Bruzual & Charlot 2003](#); [Arnouts et al. 2007](#)) and CFHTLS ([Ilbert et al. 2006](#)) samples are essentially updated and refined versions of the CWW-Kinney sample. Finally, the COSMOS sample ([Ilbert et al. 2009](#)) is based on more recent SEDs of three ellipticals and six spirals (S0, Sa, Sb, Sc, Sd, Sdm, [Polletta et al. 2007](#)), as well as 12 starbursts ([Bruzual & Charlot 2003](#)).

We conclude this section with brief notes on the redshift of individual objects.

- Both XT 161028 ( $z = 0.29$ ) and 151219 ( $z = 0.62$ ) have photometric redshifts from SDSS-IV Data

- Release 16 (Ahumada et al. 2019). We choose to adopt the SDSS values, which are very similar to the values obtained using our redshift estimation method (0.28 and 0.66, respectively). This choice does not affect the results and facilitates comparisons with other works that rely on SDSS redshifts. XT 151219 also has redshift estimates of 0.67 (Kuijken et al. 2019) and 0.68 (Wright et al. 2019) using combined data from KiDS and VIKING, 0.27 (de Jong et al. 2017) using only KiDS, and 0.61 from the Hyper Suprime-Cam Subaru Strategic Program (Nishizawa et al. 2020). Large errors for a small fraction of photometric redshift estimates are common, which we believe explains the deviating value of 0.27.
- Our SED fit results in a preliminary redshift of 0.088 for XT 110621. Additionally, it is located 11 arcsec (corresponding to a projected distance of 20 kpc at the final redshift) away from an  $m_r = 15.6$  mag<sub>AB</sub> galaxy and 44 arcsec (77 kpc) from an  $m_r = 13.4$  mag<sub>AB</sub> galaxy (Figure 1). The former has a photometric redshift of 0.097 (Dalya et al. 2016) and the latter a spectroscopic redshift of 0.095 (Jones et al. 2009). For these reasons, we adopt  $z = 0.095$  as the final value for XT 110621.
  - XT 030206 is well-fit by SB10 in the COSMOS sample, which is the second bluest starburst in the sample. Furthermore, the SED captures the Balmer break well, which no other SED type does adequately. This lends confidence to the photometric redshift and we take  $z = 1.17$  for this galaxy.
  - XT 070618 has no detected host but is located 11 arcsec (58 kpc) away from an  $m_r = 20.83$  mag<sub>AB</sub> galaxy and 21 arcsec (107 kpc) from an  $m_r = 18.8$  mag<sub>AB</sub> galaxy (Figure 1). We assume that all three sources are located at the same redshift and perform SED fits to the two bright galaxies. Reasonable agreement is achieved for  $z = 0.37$ , which we take as the estimate for XT 070618 despite the uncertainties.
  - XT 060207 lacks information for any type of redshift estimate. Therefore, we simply adopt a fiducial value of  $z = 0.3$ . This redshift results in reasonable inferred SBO parameters and is also motivated by the photometry limits on a host galaxy. A much lower redshift would require a very faint host, whereas a much higher redshift would imply an extreme X-ray transient. However, we stress

that the redshift of this transient is clearly highly uncertain.

- XT 100424 has acceptable SED fits for redshifts in the range 0.08–0.4. There are two galaxies with  $m_r = 16.0$  and 16.5, respectively, at distances of 63 arcsec (146 kpc) at  $z = 0.10$  and 71 arcsec (166 kpc) at  $z = 0.16$ . These two redshifts are photometric redshifts from the GLADE catalog (Dalya et al. 2016). We adopt a redshift of 0.13 for XT 100424 (implicitly for all three galaxies) based on the combined information.
- XT 151128 has acceptable SED fits for redshifts in the range 0.2–0.65. The best fit is around 0.48, which we adopt as the favored redshift.
- We also use the fiducial value of  $z = 0.3$  for XT 050925 and 160220. In contrast to XT 060207, there are NIR detections for these sources and  $z = 0.3$  results in reasonable host NIR absolute magnitudes.
- The redshift for XT 140811 is solely based on SED fits, which favor a redshift of 0.57.
- The redshift for XT 040610 is determined based on photometric redshifts from SDSS12 (Alam et al. 2015) of eight neighboring galaxies within 20 arcsec (123 kpc). The average redshift is 0.5 with a standard deviation of 0.17. We take  $z = 0.5$  as the redshift of XT 040610 despite the large uncertainties.

#### 4. OBSERVATIONS AND DATA REDUCTION

We perform data reduction of all selected sources (Table 1) largely following standard procedures. This data reduction is independent of the automatic processing used for finding the transients (Appendix A). We use *XMM-Newton* Science Analysis System (SAS) version 18.0.0 (Gabriel et al. 2004) and the latest CCF as of 2019 December 11. We inspect the images from the Optical Monitor (Mason et al. 2001) on board *XMM-Newton* when available, but find no variable emission that appears connected with the X-ray transients. Henceforth, we only consider data from the European Photon Imaging Camera (EPIC). All 12 sources are covered by pn and MOS2, while 8 sources are covered by MOS1 since part of its FoV has been disabled.

We apply the latest calibration using the tasks `epproc` and `emproc`. We also apply filters to keep data only in the range 0.3–10 keV with standard filtering parameters. We select temporary source regions and final background regions by hand. The background regions typically have radii of  $\sim 1$  arcmin and are selected to be

close to the source, free of other sources, and on the same CCD chip as the source. We use these source and background regions to construct preliminary light curves.

Next, we define five time intervals: before, during, after, and the first and second halves of the transient. The halves of the transient are defined to have approximately equal fluences. These two halves are only used for time-resolved spectral analysis (Section 5). All time intervals are defined by eye based on inspections of the preliminary source light curves.

We remove periods of high background before and after the defined duration of the transient following standard procedures. The background levels during the transients are not high enough to significantly affect the analysis. Only XT 110621 occurs during a high background interval, but is still clearly detected with a signal-to-noise ratio (S/N) of 5. The median S/N across all sources is 7, where the longer transients contribute to a lower ratio. We note that the S/N only includes the photon number statistics and does not represent the detection statistic, which also includes the spatial information. The lowest detection statistic as defined by `emldetect` (Watson et al. 2009) is 20 for XT 151128. This approximately corresponds to a false detection probability of  $2 \times 10^{-9}$ .

With the time intervals, it is possible to obtain an improved estimate of the source position by fitting to the image created from the duration of the transient. We use the SAS task `edetect_chain` to fit for the position in the 0.3–10 keV range in all cameras simultaneously. We add in quadrature a systematic uncertainty of 1.2 arcsec<sup>3</sup> to the statistical uncertainty from `edetect_chain`, to obtain the final position uncertainty. We adopt this position as the final source position and create the final source regions. The radii for these regions are chosen to maximize the S/N, which is computed by the SAS task `eregionanalyse`.

The next step of the data preparation is to create a light curve using the updated source region, and create images and extract spectra during each of the five time intervals. The light curve and images are created following standard *XMM-Newton* data reduction procedures. We largely follow standards when extracting the spectra as well. However, we group all source spectra to at least 1 count per spectral bin, which is necessary for using *C*-stat in XSPEC<sup>4</sup>. The ancillary re-

sponse files (ARFs) and response matrix files (RMFs) for the individual cameras are generated using the SAS tasks `arfgen` and `rmfgen`, respectively. Solely for presentation purposes, we also combine the spectra from the three cameras using `especcombine`. The individual spectra used for the merged EPIC spectra are binned using a common channel grid corresponding to uniform bins of width 0.2 keV.

To determine upper limits on the source flux during the time intervals before and after the transient, we use the SAS task `esensmap`. The task computes the photon flux required for a hypothetical source to be detected in the combination of all three instruments. To convert the photon flux to physical units, we use the best-fit model of the time-averaged spectrum (Section 5). For the upper limits, we choose a detection threshold (DET\_ML) of 5.9, which corresponds to a chance probability for detection of  $2.7 \times 10^{-3}$  ( $3\sigma$ ) under the null hypothesis.

To estimate the peak flux of each transient, we start by finding the shortest time interval during which 25 % of all source photons are detected. This is done by searching a combined EPIC source event list. Having determined the time interval with the highest photon flux, we use `epiclccorr` to apply all corrections to obtain the corrected count rate with error bars. This task is usually used to produce light curves, whereas we use it here to compute a count rate during a single time interval. This is performed on the cameras individually, with the single-bin time interval provided as input. The final step is to convert the peak count rates from `epiclccorr` to fluxes. We do this by scaling the fluxes obtained from the time-integrated spectral fits (Section 5) by the ratio of the peak to the time-averaged photon count rate.

When the flux is high, it is possible that two incident, spatially close photons are interpreted incorrectly. They could be detected as a single photon with higher energy or flagged as bad, a phenomenon referred to as pile-up. There is some potential for pile-up during the brightest phases of our transients. XT 070618 is the most likely to suffer from pile-up, with a peak count rate of 0.4 photons per frame in the pn CCD. The standard SAS method used for assessing pile-up, `epatplot`, is inconclusive because too few photons are detected during the short transient. Instead, we manually inspect the raw (ODF), calibrated (unfiltered), and final event lists and find no signs of suspected pile-up events. All light curves are practically identical, including the marginal double-peaked shape (Section 6).

Finally, we comment on the flux of the object XT 151219. It is close to (but not on) a chip gap on the pn CCD. A part of the standard procedure when creating pn spectra is to reject events close to chip gaps

<sup>3</sup> *XMM-Newton* Calibration Technical Note XMM-SOC-CAL-TN-0018

<sup>4</sup> <https://heasarc.gsfc.nasa.gov/xanadu/xspec/manual/XSappendixStatistics.html>

(FLAG==0). This is performed because of energy calibration uncertainties for events not completely contained on the chip. For this object, this means rejecting  $\sim 20\%$  of the pn events. The spectral shape is unaffected, but the overall flux is likely underestimated by  $\sim 15\%$  (the source is covered by both pn and MOS2). This does not affect any conclusions qualitatively and we do not attempt to correct for it.

## 5. SPECTRAL FITTING

We fit two simple models to the data: a blackbody (`zbody`) and power-law (`zpowerlw`) model. Both models also include an absorption component for the Milky Way absorption (`tbabs`, Wilms et al. 2000) and a redshifted absorption component (`ztbabs`) representing host galaxy absorption. The Milky Way column density is frozen to the weighted estimate of Willingale et al. (2013), whereas the redshifted column densities are fitted for. Both absorption components use the abundances of Wilms et al. (2000) and cross sections of Verner & Yakovlev (1995).

We freeze the redshifts to our estimated values (Table 2) and ignore the uncertainties that are implicitly introduced. The redshifts only have a minor impact on the fitted parameters (Section 6) but have significant implications for the inferred physical properties, which are discussed separately (Section 7.2).

The blackbody model is a simplified representation of a complete physical model for the time-integrated spectrum of a SN SBO (Section 7.1). The integrated spectra of SBOs are not expected to be perfectly thermal, but a blackbody is a reasonable approximation given the large uncertainties. Sapir et al. (2013) showed that the time-integrated spectrum of a SBO peaks at  $h\nu_{\text{peak}} = 3T_{\text{peak}}$ , where  $h\nu_{\text{peak}}$  is the photon energy at the spectral peak (measured in fluence per logarithmic frequency;  $\nu F_{\nu}$ ) and  $T_{\text{peak}}$  is the peak surface temperature. In comparison, the spectral peak of a blackbody of temperature  $T$  peaks at  $h\nu_{\text{peak}} = 2.82T$ . Therefore, the fitted temperature is a reasonable approximation of the peak surface temperature.

The interpretation of the power-law model is simpler than the interpretation of the blackbody because we only use the power law as a phenomenological model. Its purpose is to quantify the observed spectral slope by fitting for the photon index ( $\Gamma$ ). Moreover, the goodness of fit is also used for comparisons with the blackbody model.

We also fit the blackbody and power-law models to the spectra from the first and second halves of the transients. However, since the aim is to solely quantify spectral evolution, the host absorptions are frozen to the best-fit

values from the time-integrated fits. This assumes that all information about the evolution of the spectral shape is captured by the temperature or photon index.

### 5.1. Technical Aspects

We use XSPEC version 12.10.1f (Arnaud 1996) for the spectral analysis. The spectra are fitted simultaneously to data from all three EPIC CCDs in the entire 0.3–10 keV range. We do not introduce a free cross-normalization between the instruments. The relative calibration of the instruments are accurate to within 5–10% (Madsen et al. 2017; Plucinsky et al. 2017), but additional free constants between the instruments cannot be reliably constrained in a few cases of extremely few counts. The analysis is performed with the  $C$ -stat fit statistic (Cash 1979) in XSPEC, which is the  $W$  statistic when a Poissonian background is included<sup>5</sup>.

Confidence intervals for the parameter estimates are computed using the `error` command in XSPEC, which varies the fit parameters until the change in fit statistic reaches a given threshold. This assumes that the difference in fit statistic is distributed as  $\chi_q^2$  for  $q$  degrees of freedom. This is a reasonable approximation even for Poissonian data except for a small additive correction  $\propto n^{-1/2}$  for  $n$  photons (Cash 1979; Yaqoob 1998). For the time-integrated fits, there are three free parameters. An appropriate threshold for  $1\sigma$  confidence intervals and three independent parameters is a change in fit statistic of 3.5 (Avni 1976; Lampton et al. 1976; Cash 1976). Analogously, for the time-resolved fits with two free parameters, the corresponding value is 2.3. For reference, we note that X-ray analyses commonly use a critical value of 2.706, which represents the 90% interval for one parameter of interest.

The goodness of fits are computed by simulating 1000 spectra using the `fakeit` command in XSPEC. The spectra are simulated using the best-fit model at the energy resolution of the channels of the instruments. The faked spectra are then grouped to at least 1 count per bin, analogously to the real data. The models are then fitted to these spectra. The final goodness measure is represented by the fraction of fits to faked spectra with better test statistic than fits to the observed data. A good fit should on average result in a fraction of 0.5. For our purposes and given the systematic uncertainties, we consider goodness fractions relatively close to 1 as acceptable. The fit statistics and goodness measures for all fits are provided in Table C.1.

<sup>5</sup> <https://heasarc.gsfc.nasa.gov/xanadu/xspec/manual/XSappendixStatistics.html>



## 6. OBSERVED PROPERTIES

Here, we report the observed properties of the SBO candidates. These are practically independent of any modeling uncertainties. The redshifts enter into the fitted blackbody temperature and host galaxy absorption, but do not affect these values much. In Figure 1, we provide the sky images, light curves, and spectra for all SBO candidates. The purpose of the sky images is only to show the host galaxy candidates and the neighboring sources relative to the X-ray transients. Properties of the light curves and spectra are presented separately in Sections 6.1 and 6.2, respectively.

### 6.1. Light Curves

The light curves in Figure 1 show the temporal evolutions of the transients. We note the significantly different durations and timescales (Section 7.1) ranging from  $\sim 30$ – $10,000$  s. All transients show gradual rises that appear at least marginally resolved, although quite steep in some cases. In particular, no source shows a prompt ( $< 10$  s) rise followed by an immediate decay. This has important implications for interpreting the origins of the transients, since some are characterized by sharp rises (Section 8). We are not able to quantify the properties of the decaying tails accurately since all transients quickly fade below the detection limits. Dividing the light curves into different energy bands is limited by the number of photons, and does not reveal any significant behavior that is not captured by the time-resolved spectra (Section 6.2). Finally, we note in passing an apparent, curious double-peak structure in the light curves of XT 070618 and 060207. We do not consider this further since it appears statistically marginal, but a clearly double-peaked X-ray transient has previously been reported by Jonker et al. (2013).

The average fluxes, peak fluxes, and constraints before and after the transients are provided in Table 3 (with the peak fluxes determined as described in Section 4). This shows that the transients have large dynamic ranges of at least 10 in all cases and substantially higher in many cases. The constraints on the dynamic ranges are primarily limited by the telescope sensitivity.

For two of the transients, we find some evidence for emission outside the main transient event. This is the case for XT 161028, which is marginally detected after the main event. This is likely the decaying tail that extends beyond the selected time interval used to define the duration. No sub-threshold source is present before the transient and the limit indicates that any emission was lower than the marginal detection after. We also

find no indications of a source in two *XMM-Newton* observations<sup>6</sup> 14 years before the transient.

XT 151219 shows a marginal quiescent flux level before the transient. *XMM-Newton* observed this position 7 months before and 18 months after the transient<sup>7</sup>. The last observation marginally detects a flux level roughly half (consistent within uncertainties) of the level seen just before the transient. We interpret this as quiescent X-ray emission from an underlying active galactic nucleus. Using the flux measured just before the transient, the inferred 0.3–10 keV luminosity is  $(1.4 \pm 0.4) \times 10^{43}$  erg s<sup>-1</sup> for  $z = 0.62$ . No emission is detected in the earliest observation and just after the transient in the main observation. This is likely due to the limited sensitivity and inspections of the images reveal a sub-threshold source present in both cases.

### 6.2. Spectra

The time-integrated spectral fits are shown in Figure 1 and the parameters from all fits are provided in Table 4, including the time-resolved fits. Statistical measures of all fits are provided in Table C.1. All fits are acceptable, although there are indications that some spectral features are not properly captured by the simple models. We do not attempt to fit more complicated models due to the data quality and modeling uncertainties. Additionally, the sources likely evolve in time, which could introduce apparent spectral features in the time-integrated spectra.

All transients are soft but show a range of different color temperatures in the range 0.1–1 keV, or alternatively, photon indices of 2–4. We note that there is an observational bias toward soft sources due to the instrumental characteristics of *XMM-Newton* and the detection statistic, which scales with the number of photons rather than fluence. The time-resolved fits show that the evolutions generally go from harder to softer, although the significance is marginal in some cases. No source shows any significant hardening.

Overall, the power-law model seems to result in slightly better fits. It is possible that this is due to a stronger degeneracy between the photon index and host absorption than between the temperature and host absorption. This behavior can be seen from the fitted host absorption column densities, which generally are lower for the blackbody model than the power-law model. We do not attempt to evaluate if the blackbody or the power-law model is more reliable in this respect. This would require assuming an underlying SBO model,

<sup>6</sup> Observation IDs 0021140801 and 002114901.

<sup>7</sup> Observation IDs 0770380201 (before) and 0802860201 (after).

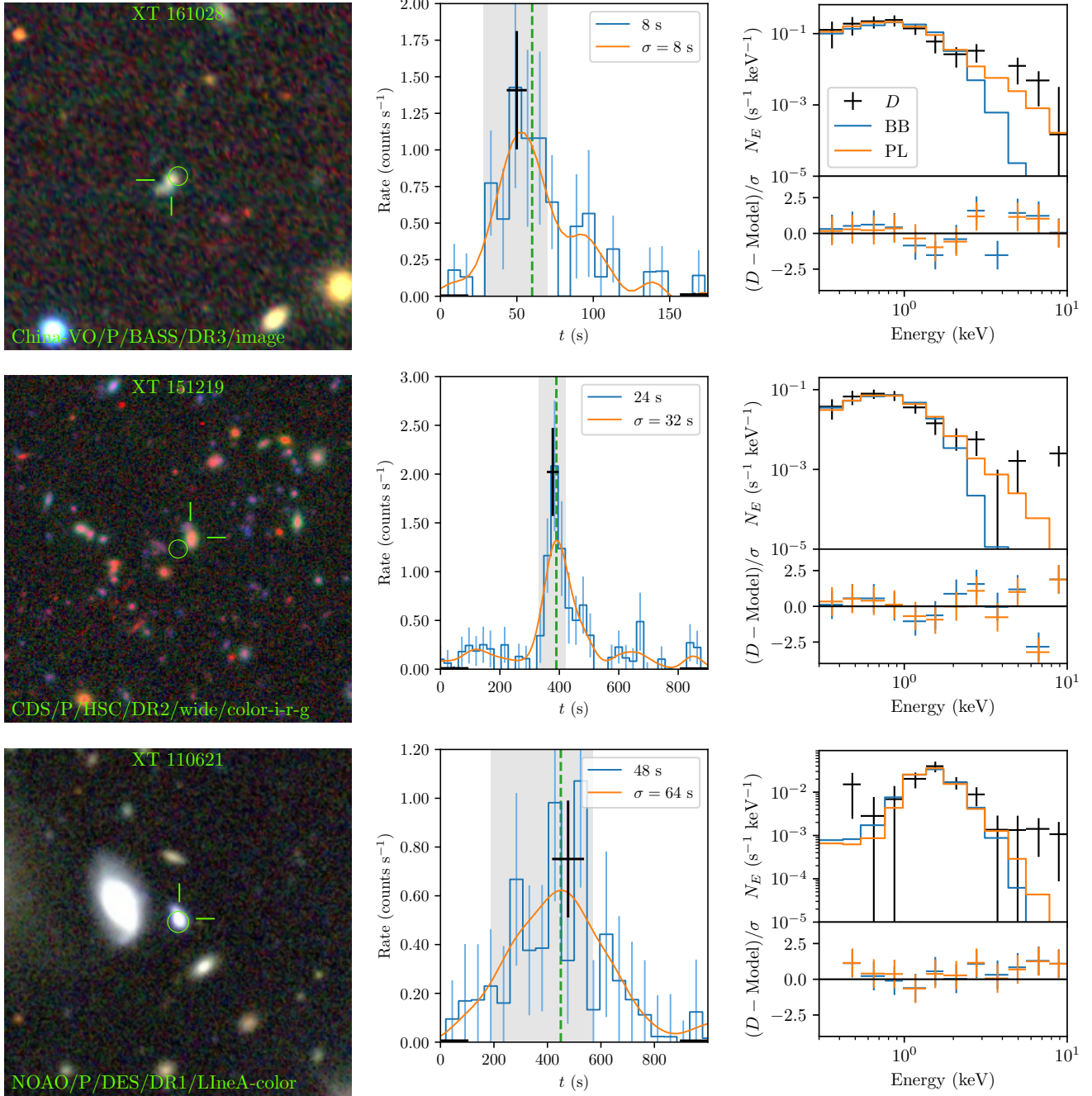


**Figure 1.** *Continues on subsequent pages (1/4).* SBO candidates in descending order of confidence of being a SN SBO. Left column: Sky images centered on the positions of the X-ray transients (green circles with  $1\sigma$  radii). The green lines mark the candidate host galaxies. The bottom texts are the sources of the images, which are all from HiPS except for VISTA and Subaru data. The color scales are arbitrary and are chosen to maximize contrast. The image colors loosely represent source colors for multi-band data. All images are  $1 \times 1$  arcmin<sup>2</sup> and the lines pointing to the galaxies are 3 arcsec. North is up and east is left. Middle column: Combined EPIC light curves in the observed 0.3–10 keV range. Blue lines are binned light curves with light blue uncertainties, and orange lines are smoothed light curves (bin sizes and kernel widths are given in the legends). The dashed green lines show the separation into first and second halves for the time-resolved spectral analysis. The gray regions show the typical timescales ( $t_{R/c}$ ; Section 7.1). The black crosses are the peak fluxes (Section 4) and the horizontal black lines (lower left and right corners, barely visible in some cases) are the flux limits (Table 3). Right column: Upper segments show the observed time-integrated spectra (black crosses) fitted with the absorbed blackbody (blue) and power-law (orange) models. Lower segments show the residuals normalized by the uncertainties using the same colors as above for the respective models. For visual clarity, we combine all EPIC data and bin to 12 energy bins logarithmically.

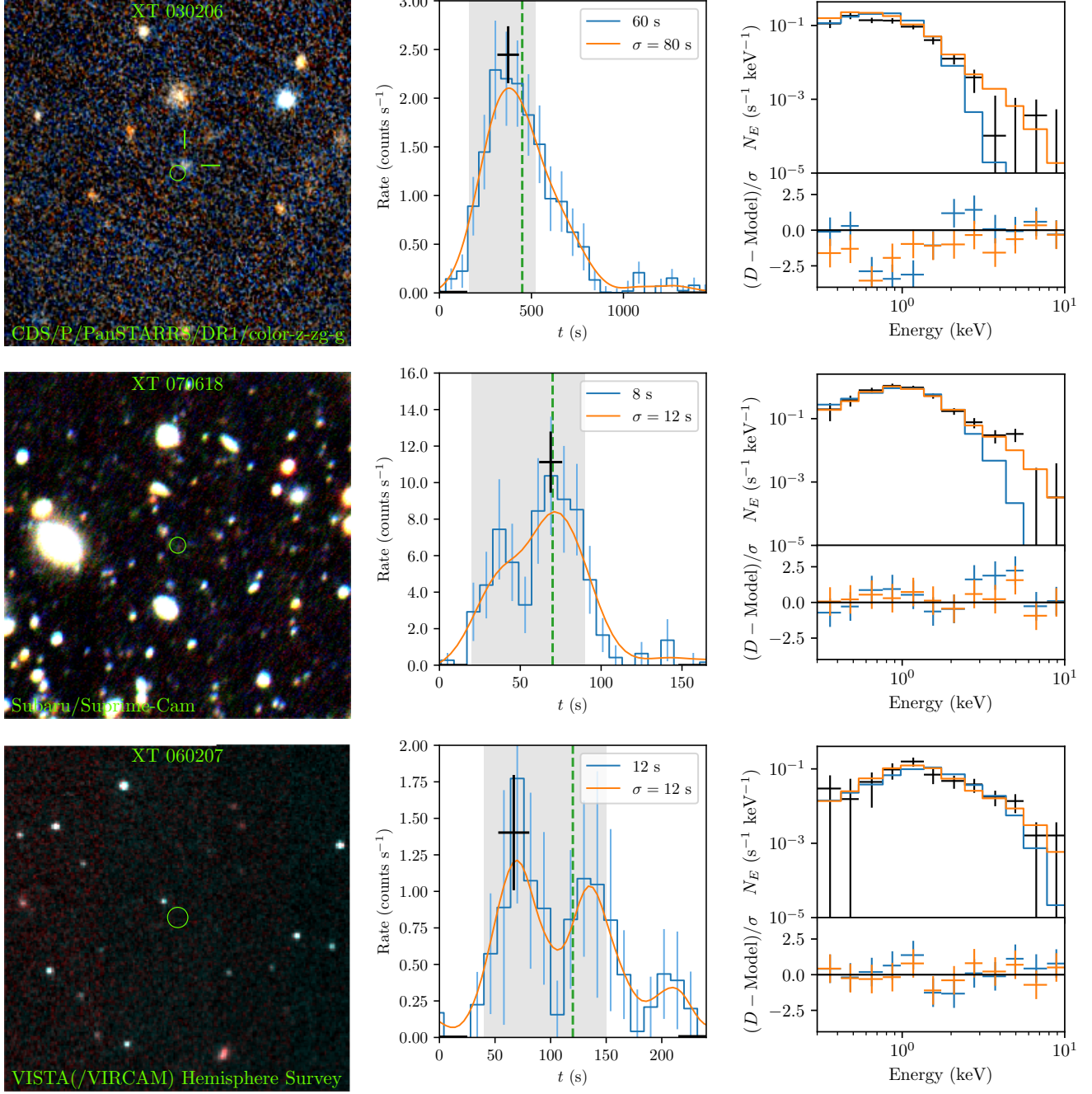
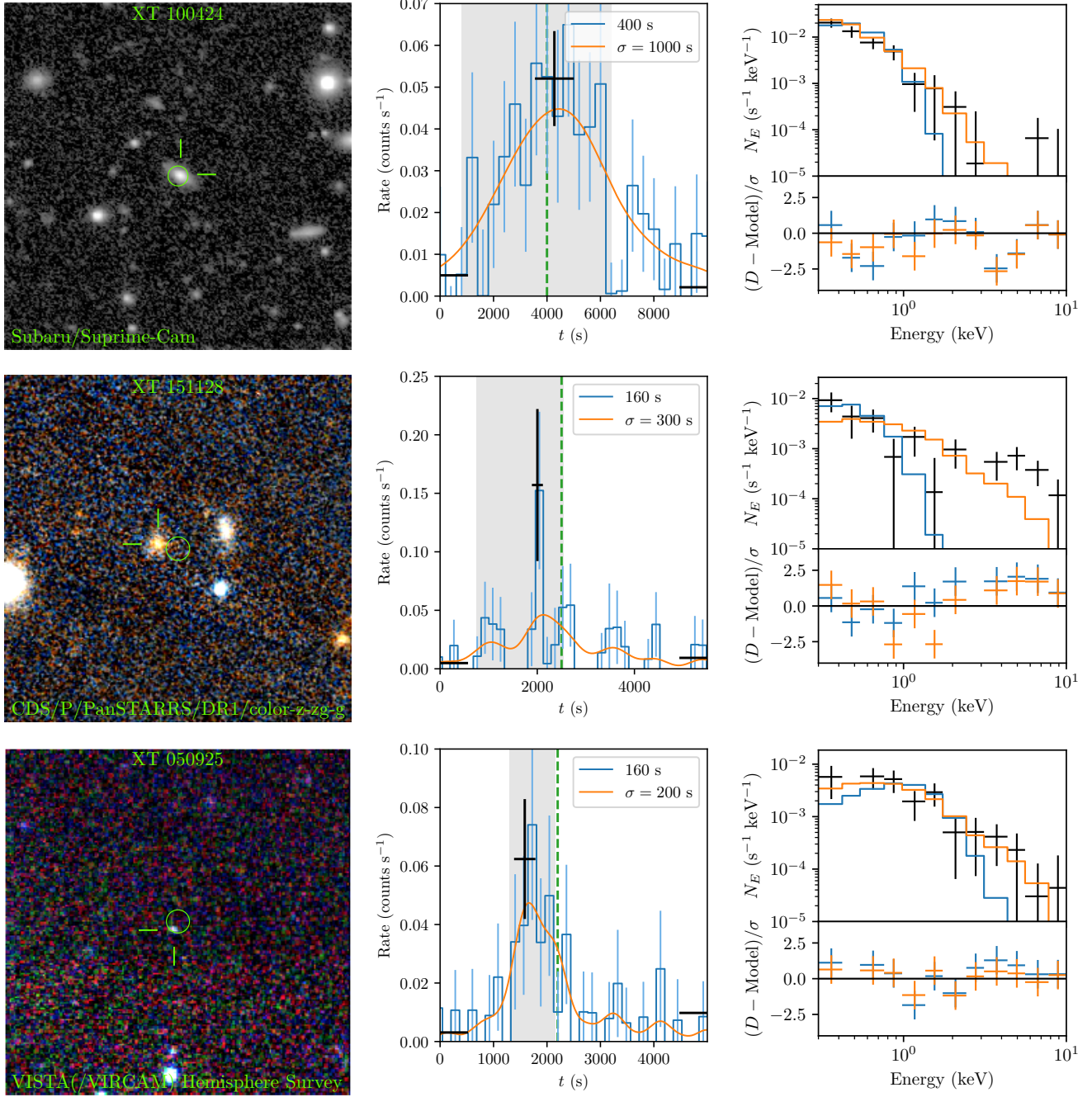


Figure 1. Continued (2/4).



Figure 1. *Continued (3/4).*

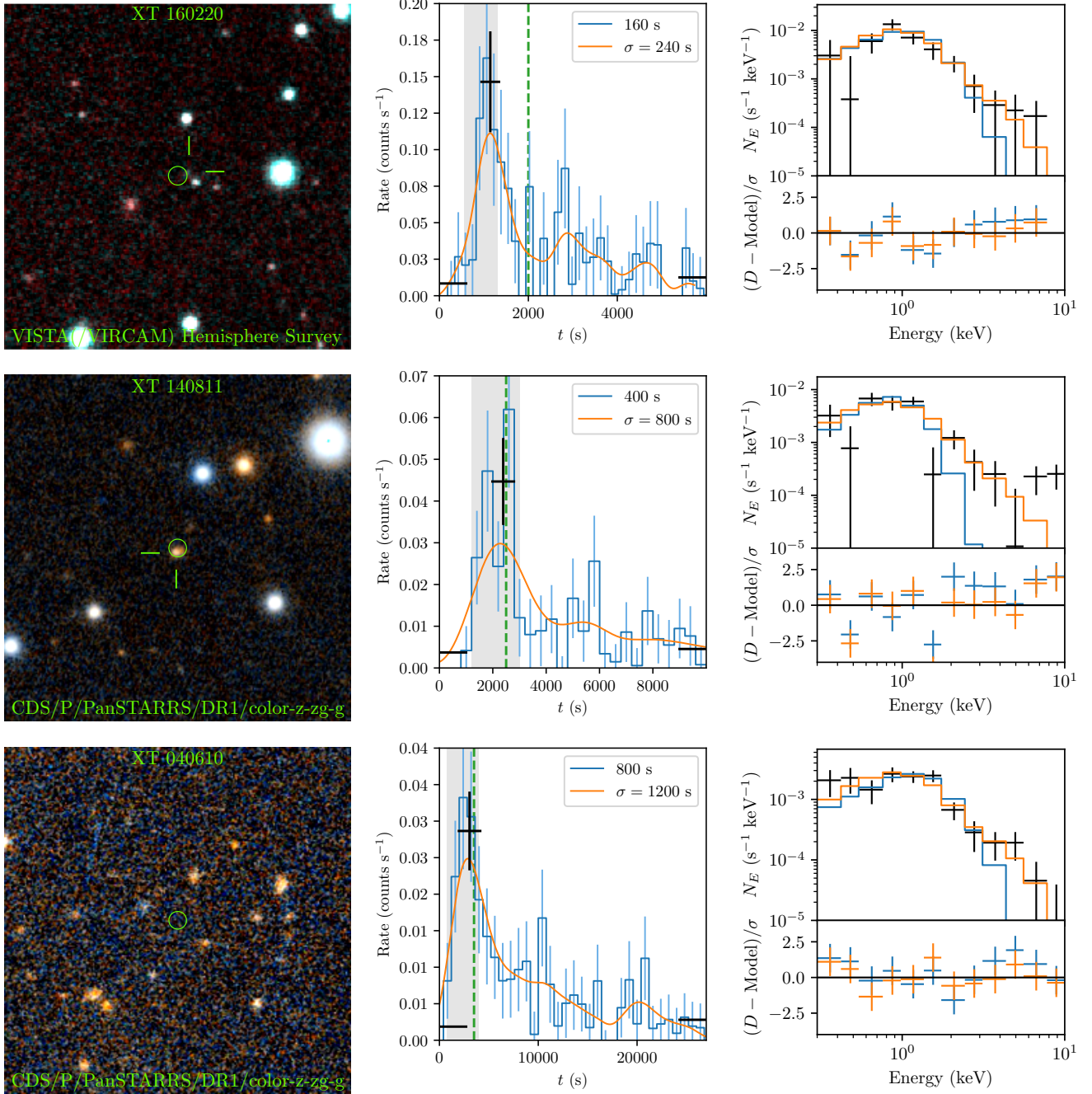
modeling the absorption of galaxies, and computing the survey sensitivity, which is beyond the scope of this paper. We simply conclude that the photon indices might be unreliable and that the degeneracy can result in apparently better fits when compared to the blackbody model. Any uncertainties in the photon indices do not affect our conclusions significantly since they are not used for inferring physical parameters.

## 7. SBO INTERPRETATION

In this section, we outline the SBO model (Section 7.1) used for inferring physical parameters from the observables (Section 7.2). We then discuss the effects of asymmetries (Section 7.3) and CSM (Section 7.4), which are not incorporated into the model. We conclude by commenting on the individual SBO candidates and how the observations compare to theory (Section 7.5).

### 7.1. SBO Model



Figure 1. *Continued (4/4).*

We use a model for SN SBOs to connect the observed properties to physical parameters of the SN and its progenitor. The aim is to infer the shock velocity ( $v_{\text{sh}}$ ), progenitor radius ( $R$ ), breakout density ( $\rho$ ), and ejecta velocity ( $v_{\text{ej}}$ ). The ejecta velocity is the typical bulk velocity defined as

$$v_{\text{ej}} = \sqrt{\frac{E_{\text{exp}}}{M_{\text{ej}}}}, \quad (1)$$

where  $E_{\text{exp}}$  is the SN explosion energy and  $M_{\text{ej}}$  the ejecta mass. The observed parameters that constrain these properties are the bolometric SBO energy ( $E_{\text{SBO}}$ ) and color temperature ( $T$ ).

Here, we closely follow the summary of SN SBO theory by Waxman & Katz (2017). For simplicity, we consider the non-relativistic regime even though BSGs are expected to be in the transitional region ( $\sim 0.1c$ ) and possibly be mildly relativistic in some cases. Non-relativistic

**Table 3.** Fluxes

XT	$F_{\text{mean}}$ ( $10^{-13}$ erg s $^{-1}$ cm $^{-2}$ )	$F_{\text{peak}}$ ( $10^{-13}$ erg s $^{-1}$ cm $^{-2}$ )	$F_{\text{before}}$ ( $10^{-13}$ erg s $^{-1}$ cm $^{-2}$ )	$F_{\text{after}}$ ( $10^{-13}$ erg s $^{-1}$ cm $^{-2}$ )	$\frac{F_{\text{peak}}}{F_{\text{before}}}$	$\frac{F_{\text{peak}}}{F_{\text{after}}}$
161028	$3.82 \pm 0.73$	$15.30 \pm 4.31$	$< 0.05$	$0.13 \pm 0.04$	$> 300$	100
151219	$2.34 \pm 0.31$	$17.61 \pm 3.82$	$0.08 \pm 0.02$	$< 0.06$	200	$> 300$
110621	$2.63 \pm 0.54$	$7.12 \pm 2.22$	$< 0.06$	$< 0.06$	$> 100$	$> 100$
030206	$5.19 \pm 0.41$	$18.79 \pm 2.15$	$< 0.07$	$< 0.02$	$> 300$	$> 800$
070618	$32.12 \pm 3.64$	$105.92 \pm 15.31$	$< 0.05$	$< 0.05$	$> 2000$	$> 2000$
060207	$10.42 \pm 1.95$	$26.25 \pm 7.23$	$< 0.08$	$< 0.15$	$> 300$	$> 200$
100424	$0.26 \pm 0.04$	$0.57 \pm 0.12$	$< 0.05$	$< 0.02$	$> 10$	$> 20$
151128	$0.27 \pm 0.06$	$2.44 \pm 0.99$	$< 0.08$	$< 0.14$	$> 30$	$> 20$
050925	$0.24 \pm 0.05$	$1.16 \pm 0.37$	$< 0.06$	$< 0.18$	$> 20$	$> 10$
160220	$0.42 \pm 0.06$	$1.92 \pm 0.44$	$< 0.11$	$< 0.16$	$> 20$	$> 10$
140811	$0.16 \pm 0.02$	$0.57 \pm 0.13$	$< 0.05$	$< 0.06$	$> 10$	$> 10$
040610	$0.12 \pm 0.01$	$0.45 \pm 0.08$	$< 0.03$	$< 0.04$	$> 20$	$> 10$

NOTE—Observed fluxes in the 0.3–10 keV range computed using the time-integrated best-fit spectrum. The choice of model is based on the goodness of fit (Table C.1). The last two columns show the dynamic ranges of the transients.

**Table 4.** Results of Spectral Fits

XT	$N_{\text{H,MW}}$ ( $10^{20}$ cm $^{-2}$ )	$N_{\text{H,BB}}$ ( $10^{22}$ cm $^{-2}$ )	$T$ (keV)	$T_1$ (keV)	$T_2$ (keV)	$N_{\text{H,PL}}$ ( $10^{22}$ cm $^{-2}$ )	$\Gamma$	$\Gamma_1$	$\Gamma_2$
161028	1.9	$< 1.2$	$0.41^{+0.17}_{-0.12}$	$0.53^{+0.20}_{-0.12}$	$0.28^{+0.11}_{-0.07}$	$< 2.2$	$2.8^{+1.8}_{-1.1}$	$2.5^{+0.7}_{-0.7}$	$3.7^{+1.3}_{-1.1}$
151219	2.5	$< 1.8$	$0.37^{+0.13}_{-0.11}$	$0.45^{+0.15}_{-0.09}$	$0.30^{+0.08}_{-0.05}$	$0.8^{+1.0}_{-0.6}$	$3.5^{+2.1}_{-1.2}$	$3.0^{+0.7}_{-0.6}$	$4.3^{+0.9}_{-0.8}$
110621	3.0	$1.3^{+3.4}_{-1.2}$	$0.42^{+0.27}_{-0.21}$	$0.52^{+0.18}_{-0.13}$	$0.26^{+0.11}_{-0.07}$	$3.4^{+3.9}_{-2.0}$	$> 2.9$	$4.1^{+1.2}_{-1.1}$	$> 5.5$
030206	6.4	$< 0.4$	$0.47^{+0.05}_{-0.05}$	$0.53^{+0.06}_{-0.06}$	$0.38^{+0.05}_{-0.05}$	$0.6^{+0.5}_{-0.5}$	$3.4^{+0.6}_{-0.5}$	$3.3^{+0.3}_{-0.3}$	$3.9^{+0.5}_{-0.5}$
070618	1.6	$< 0.8$	$0.46^{+0.10}_{-0.09}$	$0.64^{+0.12}_{-0.10}$	$0.31^{+0.05}_{-0.04}$	$0.8^{+0.5}_{-0.3}$	$3.2^{+0.8}_{-0.7}$	$2.5^{+0.3}_{-0.3}$	$4.4^{+0.6}_{-0.5}$
060207	10.8	$< 1.6$	$0.93^{+0.26}_{-0.21}$	$0.89^{+0.33}_{-0.20}$	$0.62^{+0.24}_{-0.14}$	$< 3.9$	$1.9^{+1.0}_{-0.8}$	$1.8^{+0.7}_{-0.7}$	$2.4^{+0.8}_{-0.7}$
100424	5.1	$< 0.6$	$0.13^{+0.03}_{-0.03}$	$0.13^{+0.04}_{-0.03}$	$0.12^{+0.03}_{-0.03}$	$< 0.7$	$3.9^{+2.8}_{-0.6}$	$4.0^{+1.1}_{-0.9}$	$4.1^{+0.9}_{-0.7}$
151128	5.1	$< 4.2$	$0.16^{+0.14}_{-0.11}$	$0.09^{+0.06}_{-0.03}$	...	$< 0.9$	$1.9^{+3.2}_{-1.1}$	...	$1.4^{+1.6}_{-1.4}$
050925	4.3	$< 1.9$	$0.45^{+0.36}_{-0.17}$	$0.40^{+0.23}_{-0.12}$	$0.59^{+0.95}_{-0.37}$	$< 2.4$	$2.1^{+1.6}_{-0.8}$	$2.2^{+0.8}_{-0.7}$	$1.8^{+1.2}_{-1.2}$
160220	8.4	$< 1.1$	$0.45^{+0.13}_{-0.11}$	$0.40^{+0.15}_{-0.08}$	$0.47^{+0.14}_{-0.10}$	$0.5^{+0.7}_{-0.4}$	$2.9^{+1.4}_{-0.9}$	$3.0^{+0.7}_{-0.6}$	$2.9^{+0.7}_{-0.6}$
140811	11.2	$< 4.7$	$0.32^{+0.17}_{-0.13}$	$0.38^{+0.16}_{-0.09}$	$0.28^{+0.06}_{-0.05}$	$< 3.7$	$2.7^{+2.0}_{-0.9}$	$2.5^{+0.9}_{-0.7}$	$3.0^{+0.7}_{-0.6}$
040610	4.2	$< 0.9$	$0.68^{+0.17}_{-0.13}$	$0.96^{+0.30}_{-0.20}$	$0.60^{+0.14}_{-0.11}$	$0.4^{+0.7}_{-0.4}$	$2.1^{+0.7}_{-0.6}$	$1.8^{+0.5}_{-0.5}$	$2.3^{+0.4}_{-0.4}$

NOTE—Parameters without integer subscripts are for the time-integrated spectra. The subscripts 1 and 2 refer to the first and second intervals of the time-resolved analysis, respectively. The Galactic absorptions ( $N_{\text{H,MW}}$ ) are frozen during the fits. The absorption column densities  $N_{\text{H,BB}}$  and  $N_{\text{H,PL}}$  are the redshifted host galaxy absorptions from the blackbody and power-law fits, respectively. Parameter estimates are missing for unconstrained fits.

SBOs are also more accurately modeled from a theoretical perspective. More detailed SBO modeling is not motivated due to the limited data and uncertainties in the redshifts.

The bolometric SBO energy is given by Equation (31) of Waxman & Katz (2017)

$$E_{\text{SBO}} = 2.2 \times 10^{47} R_{13}^2 v_{\text{sh},9} \kappa_{0.34}^{-1} \text{ erg}, \quad (2)$$

where  $10^n Q_n \text{ cgs} = Q$  in general for integer  $n$  and  $0.34 \kappa_{0.34} \text{ cm}^2 \text{ g}^{-1} = \kappa$  is the opacity. The opacity is given by  $\kappa = (1 + X)/5 \text{ cm}^2 \text{ g}^{-1}$ , where  $X$  is the H mass fraction. This implies that  $\kappa$  ranges from  $0.2 \text{ cm}^2 \text{ g}^{-1}$  (H-poor) to  $0.34 \text{ cm}^2 \text{ g}^{-1}$  (H-rich). The shock velocity is given by Equation (27) of Waxman & Katz (2017)

$$\frac{v_{\text{sh}}}{v_{\text{ej}}} = 13 M_{\text{ej},10}^{0.16} v_{\text{ej},8.5}^{0.16} R_{12}^{-0.32} \kappa_{0.34}^{0.16} f^{-0.05}, \quad (3)$$

where  $3000 v_{\text{ej},8.5} \text{ km s}^{-1} = v_{\text{ej}}$  and  $f$  is a numerical factor of order unity that depends on the detailed envelope structure (Appendix A of Calzavara & Matzner 2004). The numerical factor for BSGs is given by Equation (37) of Sapir et al. (2013)

$$f = 0.072 \mu_{0.62}^4 L_{\star,5}^{-1} M_{\text{ej},10}^3 \kappa_{0.34}^{-1} \times \left( 1.35 - 0.35 L_{\star,5} M_{\text{ej},10}^{-1} \kappa_{0.34} \right)^4, \quad (4)$$

where  $0.62 \mu_{0.62} = \mu$  is the mean molecular weight and  $L_{\star}$  the progenitor luminosity. The parameter  $\mu$  is given by  $\mu = (2X + 0.75Y)^{-1}$ , where  $Y$  is the He mass fraction. Although the time-integrated color temperature cannot be expressed analytically, it can be fitted by Equation (50) of Waxman & Katz (2017)

$$\log_{10} \left( \frac{3T}{\text{eV}} \right) = 1.4 + v_{\text{sh},9}^{0.5} + (0.25 - 0.05 v_{\text{sh},9}^{0.5}) \log_{10}(\rho_{-9}), \quad (5)$$

where  $\rho$  is given by Equation (28) of Waxman & Katz (2017)

$$\rho = 8 \times 10^{-9} M_{\text{ej},10}^{0.13} v_{\text{ej},8.5}^{-0.87} R_{12}^{-1.26} \kappa_{0.34}^{-0.87} f^{0.29} \text{ g cm}^{-3}. \quad (6)$$

The observed data are not able to constrain all parameters, in particular those that the observables are relatively insensitive to. Therefore, we take some values based on SN 1987A because SBOs should be most easily detectable from BSGs similar to SN 1987A (Sapir et al. 2013; Sapir & Halbertal 2014; Waxman & Katz 2017). Specifically, we assume  $M_{\text{ej}} = 15 M_{\odot}$  (Utrobin et al. 2019; Menon et al. 2019; Alp et al. 2019),  $L_{\star} = 150,000 L_{\odot}$  (Woosley et al. 1987), and a H-rich surface composition of  $X = 0.7$  and  $Y = 0.3$ . To illustrate

the weak dependence on these parameters, we note that choosing a H-poor star with a factor of 10 lower  $M_{\text{ej}}$  and a factor of 10 higher  $L_{\star}$  only changes  $R$  by a factor of 0.83,  $v_{\text{sh}}$  by 0.86,  $\rho$  by 4.0, and  $v_{\text{ej}}$  by 1.7. With the fiducial SN 1987A values, Equations (2), (3), (5), and (6) form a system of equations with 4 unknowns. The solution process can be simplified by solving Equation (3) for  $v_{\text{ej}}$ , inserting it into Equation (6), and using Equation (2) to express  $\rho$  in terms of  $E_{\text{SBO}}$ , which results in

$$\rho = 5 \times 10^{-9} E_{\text{SBO},46}^{-0.75} \text{ g cm}^{-3} \quad (7)$$

for our assumed parameter values.

In addition to the constraint on  $R$  from the model above, an independent constraint can be placed based on the light curve. The light curve shape is initially determined by the light travel time from different parts of the progenitor. The light curve rises and remains approximately constant until a time of  $t_{R/c} \equiv R/c$ , after which it starts decaying (Nakar & Sari 2010). This light travel time argument only applies if the SBO is at least approximately spherical. Furthermore, it is only valid if  $t_{R/c}$  is longer than the dynamical time of the breakout shell (breakout shell width over  $v_{\text{sh}}$ ). This is expected to be the case for all but the most extended RSGs, which are likely to be too cool to be observed.

## 7.2. Inferred SN Properties

Here, we use the model outlined above to infer physical SN parameters, which are provided in Table 5. The table includes values that are derived using both the energetics and the light curve shape. The primary goal is to determine if the obtained parameters are consistent with typical SN SBO values. This is mainly relying on comparisons with theoretical predictions due to the lack of observations. We do not attempt to model and propagate all uncertainties into these parameters. However, we stress that both the redshift (Section 3) and modeling uncertainties are large. More detailed analyses of the transients require spectroscopic redshifts and will be the subject of future studies.

From the light curves (Figure 1), we define the typical timescales by hand, as described above. We denote radii determined using this method  $R_t$  to distinguish  $R_t$  from the radii inferred from the energetics, which we denote  $R_E$ .

The peak luminosities ( $L_{\text{peak}}$ ) and total SBO energies ( $E_{\text{SBO}}$ ) rely on the redshift estimates and extrapolations of the spectra. We use the time-integrated best-fit blackbody models to extrapolate from the observed 0.3–10 keV range to obtain the bolometric quantities. For the typical best-fit temperatures of  $\sim 0.4$  keV, the 0.3–10 keV range already captures the vast majority of

**Table 5.** Inferred SBO Properties

XT	$t_{R/c}$	$L_{\text{peak}}$	$E_{\text{SBO}}$	$R_t$	$R_E$	$v_{\text{sh}}$	$v_{\text{ej}}$	$\rho$	$E_{\text{exp}}$
	(s)	( $10^{44}$ erg s $^{-1}$ )	( $10^{46}$ erg)	( $R_{\odot}$ )	( $R_{\odot}$ )	( $10^3$ km s $^{-1}$ )	( $10^3$ km s $^{-1}$ )	( $10^{-9}$ g cm $^3$ )	( $10^{51}$ erg)
161028	42	$3.39^{+2.40}_{-1.03}$	$0.3^{+0.2}_{-0.1}$	14	11	22	1.5	13.0	0.7
151219	90	$32.88^{+53.76}_{-11.00}$	$2.4^{+4.0}_{-0.8}$	24	30	25	2.2	2.5	1.4
110621	380	$0.39^{+7.45}_{-0.22}$	$0.5^{+9.5}_{-0.3}$	150	14	24	1.7	8.2	0.9
030206	360	$172.47^{+28.72}_{-23.77}$	$79.0^{+13.2}_{-10.9}$	71	146	35	4.5	0.2	6.0
070618	70	$48.78^{+17.05}_{-10.68}$	$7.6^{+2.6}_{-1.7}$	22	49	30	2.9	1.1	2.6
060207	110	$6.44^{+2.74}_{-2.03}$	$2.2^{+0.9}_{-0.7}$	36	23	39	3.0	2.8	2.6
100424	5600	$0.05^{+0.12}_{-0.01}$	$1.0^{+2.6}_{-0.3}$	2136	30	11	1.1	4.9	0.3
151128	1800	$1.83^{+56.98}_{-1.08}$	$2.5^{+78.1}_{-1.5}$	524	41	14	1.5	2.5	0.6
050925	850	$0.21^{+0.14}_{-0.08}$	$0.3^{+0.2}_{-0.1}$	282	10	24	1.6	12.9	0.7
160220	750	$0.51^{+0.23}_{-0.12}$	$0.6^{+0.3}_{-0.2}$	249	16	25	1.8	6.9	1.0
140811	1800	$0.93^{+4.64}_{-0.41}$	$2.9^{+14.6}_{-1.3}$	494	34	23	2.1	2.2	1.3
040610	3200	$0.32^{+0.09}_{-0.07}$	$1.8^{+0.5}_{-0.4}$	919	23	34	2.6	3.1	2.0

NOTE—Timescales ( $t_{R/c}$ ) are defined by hand (Section 7.1) and are given in the observer frame. The redshift correction is applied when computing the radius  $R_t = ct/(1+z)$ . The luminosities and energies are bolometric. The parameters  $L_{\text{peak}}$  and  $E_{\text{SBO}}$  are observational and do not rely on the SBO modeling. The intervals for  $L_{\text{peak}}$  and  $E_{\text{SBO}}$  only represent the X-ray fitting uncertainties and do not include the redshift uncertainties. The large uncertainties for XT 151128 are due to a combination of few photons and a low lower temperature limit. We refrain from estimating the uncertainties for the remaining parameters since they include uncertainties in the redshifts as well as the SBO modeling, which are difficult to quantify (Sections 3 and 7.1).

the bolometric flux. The time-averaged luminosities obtained from the fits are scaled to the light curve peaks using the peak-to-average flux ratio (Section 4; Table 3). Having computed the energy  $E_{\text{SBO}}$ , it is straightforward to solve for the remaining parameters (Section 7.1). Finally, we note that  $L_{\text{peak}}$  is more uncertain than  $E_{\text{SBO}}$ , both from an observational and theoretical perspective. Therefore, we focus on  $E_{\text{SBO}}$  for the current analysis and provide  $L_{\text{peak}}$  solely for comparisons with other X-ray transients in general.

The parameter values in Table 5 are in reasonable agreement with predictions for SN SBOs. For reference, we compute the expected values for a SBO similar to SN 1987A. In addition to the assumed values in Section 7.1, we complete the model by taking  $R = 40 R_{\odot}$  and  $E_{\text{exp}} = 1.5 \times 10^{51}$  erg (McCray 1993). For this set of parameters, the derived properties are:  $E_{\text{SBO}} = 4.0 \times 10^{46}$  erg,  $v_{\text{sh}} = 23,000$  km s $^{-1}$ ,  $v_{\text{ej}} = 1800$  km s $^{-1}$ , and  $\rho = 1.7 \times 10^{-9}$  g cm $^{-3}$ .

The values for  $E_{\text{SBO}}$ ,  $R_E$ ,  $\rho$ , and  $E_{\text{exp}}$  are generally within an order of magnitude of the predicted values. These are dependent and primarily show that the observed  $E_{\text{SBO}}$ , and to a lesser extent  $T$ , are within the range of predictions for SBOs. Estimates of  $v_{\text{sh}}$  and  $v_{\text{ej}}$  are more closely clustered around 20,000 km s $^{-1}$  and 2000 km s $^{-1}$ , respectively. This is expected because the

velocities are mainly constrained by, and quite insensitive to,  $T$  through Equations (3) and (5). This implies that most soft spectra would result in reasonable  $v_{\text{sh}}$  and  $v_{\text{ej}}$ . Furthermore, there is a strong observational bias against detecting objects cooler than 0.1 keV because of the lower 0.3 keV energy limit of *XMM-Newton* and ISM absorption.

It is worth pointing out that the independent estimates of  $R$  are within a factor of  $\sim 2$  for 5 of the sources. These two estimates are completely independent and lend some strength to the SBO interpretation. The remaining objects all have substantially larger  $R_t$  than  $R_E$ . This is a consequence of the observed timescale being longer than the expected timescale. Possible reasons for longer timescales are asymmetries and dense CSM structures, as discussed below.

### 7.3. Asymmetries

Strong asymmetries in core-collapse SNe are predicted from theory (Janka et al. 2016; Müller 2016; Couch 2017) and clearly supported by observations (Larsson et al. 2016; Abellán et al. 2017; Grefenstette et al. 2017). Asymmetric SBOs have been studied (Suzuki & Shigeyama 2010; Couch et al. 2011), but have relied on bimodal, jet-like, two-dimensional axisymmetric explosions. These asymmetries were introduced by



hand but showed that asymmetries could contribute to longer timescales and significantly affect the light curve shape. To first order, the asymmetries only affect when the shock reaches the surface. The minor differences in shock velocity and breakout angle should have much smaller effects on the SBO properties. This means that only the light curve shape should be affected by the asymmetries.

More recently, [Wongwathanarat et al. \(2015\)](#) performed self-consistent three-dimensional neutrino-driven SN simulations to late times past SBO (Figure 14 of [Wongwathanarat et al. 2015](#)). They used a set of RSG and BSG single-star progenitors and have now also studied BSGs that are the results of binary mergers ([Menon & Heger 2017](#); [A. Wongwathanarat 2020](#), private communication). Although these simulations do not compute the SBO emission, they track the shock as it propagates through the star and breaks the surface. For the single-star BSG progenitor B15, the time difference between the first and last parts of the shock breaking the surface is approximately 200 s. This is a relatively spherical model. The BSG merger progenitors are more asymmetric and show time differences of  $\sim 1000$  s. These values can be compared to the times required for the shock to propagate through the stars of 4500–7500 s. For W15, which is a relatively asymmetric RSG, the fastest shock breaks out at  $\sim 70,000$  s and the slowest at  $\sim 83,000$  s post-bounce.

We emphasize that these asymmetries are not introduced by hand and develop spontaneously during the explosion from initial seed perturbations. This implies that asymmetries are expected to develop even for spherical progenitors. It is also worth pointing out that aspherical SBOs could both shorten or lengthen the observed timescale, depending on the viewing angle.

To summarize, it is likely that asymmetric shocks develop during the core-collapse process. These asymmetries significantly affect the duration and light curve shape of the observed SBO. We tentatively conclude that asymmetries can introduce time variations of up to 20 % of the shock crossing time of the star, which is an order of magnitude longer than the light crossing time  $R/c$  in extreme cases. The effects of asymmetries on the timescale are sufficient to reduce the tensions between  $R_t$  and  $R_E$  in the cases where they are significantly different.

#### 7.4. Circumstellar Medium

The CSM affects the SBO emission if the optical depth of the CSM is larger than  $c/v_{\text{sh}}$ . In these cases, the shock does not break out at the surface, but instead propagates into the CSM. A notable example is the initial X-ray transient associated with SN 2008D ([Soderberg](#)

[et al. 2008](#)), which is particularly interesting because of similarities with some of our SBO candidates. For reference, the SN 2008D SBO had a peak luminosity of  $4 \times 10^{43}$  erg s $^{-1}$ , total energy of  $6 \times 10^{45}$  erg, a timescale of  $t_{R/c} \approx 150$  s, and a  $\Gamma \approx 2$  power-law spectrum ([Modjaz et al. 2009](#)). A thermal spectrum with a temperature of 0.75 keV fits the data worse but is still statistically acceptable. From these values and using our methods, we would infer  $R_t = 65 R_\odot$  and  $R_E = 11 R_\odot$ .

A common interpretation of the SN 2008D X-ray transient is a SBO from the explosion of a WR star surrounded by a thick wind ([Chevalier & Fransson 2008](#); [Balberg & Loeb 2011](#); [Svirski & Nakar 2014](#)). CSM SBOs are also often used to explain observations of Type II $n$  and super-luminous SNe (Section 6.1 of [Waxman & Katz 2017](#) and references therein). However, these SBOs are very different and are not expected to appear as X-ray transients on timescales that our searches are sensitive to.

We do not attempt to explore the effects of a dense CSM in detail due to the wide range of possible scenarios and the observational uncertainties. Instead, we simply note that a dense CSM could increase the timescale and that some of our candidates are similar to SN 2008D.

#### 7.5. Notes on Individual Objects

Even though the inferred parameters (Table 5) agree reasonably well with theoretical predictions, there are some aspects that cause tensions with a clean SBO interpretation. In light of the discussions of asymmetries and effects of the CSM, we provide more detailed comments on individual objects below.

- The first two objects, XT 161028 and 151219, agree very well with BSG SBO predictions. The derived quantities are close to fiducial SBO values under the assumptions of spherical symmetry and thin CSM. The only parameter that stands out is  $E_{\text{SBO}}$  for XT 161028, which is an order of magnitude lower than the reference value. Given the uncertainties, we do not consider this to be a major problem and conclude that both objects are strong SN SBO candidates.

- All properties of XT 110621<sup>8</sup> agree well with predictions for BSG SBOs, except for the timescale. This can be seen from the discrepancy between  $R_t = 150$  and  $R_E = 14$ . One possible explanation for the longer observed timescale is an asymmetric BSG SBO. Another possibility is a SBO from a WR with a dense wind, similar to the SN 2008D SBO. They both have practically the same peak luminosities and total energies, although the light curve shapes are slightly different and XT 110621 has a softer spectrum. Given the expected variances in light curves and spectra, a similar origin for XT 110621 is possible. We are not able to distinguish between an asymmetric BSG SBO and a dense CSM WR SBO, but conclude that both are possible origins.
- XT 030206 is the most energetic object and would require extreme SN parameters. Interestingly, the inferred  $E_{\text{exp}}$  of  $6 \times 10^{51}$  erg is in the range of  $(7.1 \pm 5.4) \times 10^{51}$  erg typical of Type Ic-BL SNe (Taddia et al. 2019). Our modeling does not strictly apply to these SNe and any firm conclusions would require further analysis (Section 8.2).
- Both XT 070618 and 060207 agree well with the BSG SBO interpretation. The main uncertainty for these objects is due to the lack of host detections. This implies that the redshift estimates are highly uncertain, which propagates into all inferred parameters.
- XT 100424 and 151128 are the coolest objects and are much slower than expected for typical SBOs from BSGs. The observed properties suggest that they might instead be associated with SBOs from RSGs. A less explored possibility is SBOs from yellow supergiants (Smartt 2009; Ergon et al. 2014), which in the current context effectively is an intermediate class between RSGs and BSGs. The interpretations for these two objects are mainly driven by the timescales and temperatures, which are observationally reliable. The total energies are more than an order of magnitude

lower than predicted for RSG SBOs, but are uncertain due to the observed energy range relative to the temperatures, as well as the redshift uncertainties. The transients are also hotter than RSG SBO predictions, but this is anticipated because of the very strong observational biases against the cooler majority of RSG SBOs. The timescales are also slightly longer than expected, but this can be alleviated by invoking asymmetries.

- The last four transients, XT 050925, 160220, 140811, and 040610 have longer timescales than expected for BSG SBOs. They are all largely similar to XT 110621 (and implicitly also the SN 2008D SBO) and the same arguments apply to these four sources. The main differences for these last four transients are the uncertain host redshifts and the risk of being foreground contamination (Section 8.1).

## 8. ALTERNATIVE EXPLANATIONS

In this section, we explore possible sources other than SNe that could produce the observed transients. Section 3 of Bauer et al. (2017) provides a similar discussion with a slightly different focus. They discuss CDF-S XT1, which suffers from similar potential contaminants as our SBO candidates. The most likely sources to be confused for SN SBOs are flares from Galactic late-type dwarfs (Section 8.1). We discuss GRBs as potential sources in Section 8.2 and a number of less probable sources in Section 8.3. We note that the predicted number of SN SBOs (Sapir & Halbertal 2014; Waxman & Katz 2017) is comparable to the number we observe, which lends strength to the SBO interpretation.

### 8.1. Dwarf Stars

X-ray flares from late-type dwarf stars (Güdel 2004; Güdel & Nazé 2009; Benz & Güdel 2010) could potentially be confused for SBO candidates, in cases where a host galaxy is not clearly detected. The coolest object observed to flare in X-rays is an L1 dwarf (De Luca et al. 2020). A qualitative difference between SN SBOs and dwarf flares is that dwarf flares are recurrent (and any dwarfs with multiple flares would already have been excluded from our sample). Faint flares are frequent and occur up to tens of times per day, while the rate of the most powerful flares are limited by the observed sample size (Lloyd et al. 2018a,b).

The distribution of peak X-ray (0.3–10 keV) luminosities of dwarf flares extends to  $\sim 10^{30}$  erg s<sup>−1</sup> and decreases steeply with peak flux (Cook et al. 2014; Williams et al. 2014; Lloyd et al. 2018a,b; De Luca et al. 2020). The effective temperatures for the majority of

<sup>8</sup> After submission of our paper, Novara et al. (2020) reported an independent discovery of XT 110621 (EXMM 023135.0–603743 using their notation). Importantly, they find a spectroscopic redshift of 0.092 for the host galaxy (compared to our value of 0.095), which eliminates much of the uncertainty for our analysis of XT 110621. Overall, their and our results and interpretations agree very well with each other. There are minor differences in the spectral fits, which likely are due to a combination of different methods, the high background (Section 4), and the high host absorption.

the flares are in the range  $\sim 0.5\text{--}2$  keV (Pallavicini et al. 1990; Robrade & Schmitt 2005; Pye et al. 2015; De Luca et al. 2020). Typical timescales range from a few hundred to a few thousand seconds, and the dynamic ranges vary from a factor of 2 to more than 300 (Favata et al. 2000; Pandey & Singh 2008; Robrade et al. 2010; Pye et al. 2015).

For our purposes, we focus on the extreme cases despite their low rates. The 2014 April 23 flare from DG CVn is the most luminous observed M dwarf flare (Caballero-García et al. 2015; Osten et al. 2016). DG CVn is a binary system composed of two M4Ve dwarfs with a combined absolute  $J$ -band magnitude of 7.2 mag<sub>AB</sub>. The flare reached a peak flux of  $3 \times 10^{32}$  erg s<sup>−1</sup> and the dominant flare component evolved on a timescale of  $\sim 300$  s. Another comparable event is the 2008 April 25 EV Lac flare (Osten et al. 2010). EV Lac is an M3.5V dwarf with an absolute  $J$ -band magnitude of 8.5 mag<sub>AB</sub>. The X-ray flare reached a peak flux of  $10^{32}$  erg s<sup>−1</sup> and the dominant component evolved on a timescale of  $\sim 300$  s. However, these events are very hard, with peak temperatures of 25 keV (DG CVn) and 10 keV (EV Lac), and even triggered the gamma-ray burst monitor *Swift*/BAT (Barthelmy et al. 2005). The L1 dwarf flare reported by De Luca et al. (2020) reached a peak flux of  $6.3 \times 10^{29}$  erg s<sup>−1</sup>, had a temperature of 1.4 keV, and evolved on timescales of  $\sim 3$  ks. The absolute  $J$ -band magnitude of the L1 dwarf is 12.8 mag<sub>AB</sub>. Finally, we note that Glennie et al. (2015) report a tentative association of an X-ray transient with an L1 dwarf. The inferred peak luminosity is  $7 \times 10^{31}$  erg s<sup>−1</sup>; however, both the spectral type and distance to the source are uncertain.

We can use the optical and NIR data (Table B.1) to constrain the distance to a potential dwarf star. This can be combined with the peak X-ray fluxes (Table 3) to infer a peak X-ray luminosity if the source is a dwarf. For reference, the X-ray luminosity expressed in terms of peak flux ( $F_{-13} = 10^{13} F_{\text{peak}}$  erg s<sup>−1</sup> cm<sup>−2</sup>), apparent magnitude ( $m$ ), and absolute magnitude ( $M$ ) is

$$L_{\text{peak}} = 1.2 F_{-13} \times 10^{27+0.4 \times (m-M)} \text{ erg s}^{-1}. \quad (8)$$

The peak flare flux relative to absolute magnitude is comparable for M and L dwarfs. For the discussion, we adopt fiducial dwarf absolute magnitudes of  $M_r = 9$  mag<sub>AB</sub> (Bochanski et al. 2011; Pecaut & Mamajek 2013) and  $M_J = 8$  mag<sub>AB</sub> (Pecaut & Mamajek 2013; Carnero Rosell et al. 2019), which are representative of an M4 dwarf, and similarly for an L1 dwarf:  $M_z = 14.3$  mag<sub>AB</sub> (Carnero Rosell et al. 2019; De Luca et al. 2020) and  $M_J = 13$  mag<sub>AB</sub>.

For two of the three candidates without hosts, XT070618 and XT060207, the inferred luminosities are orders of magnitude higher than what have been observed from dwarf stars. For the last candidate without a host, XT040610, the observations are marginally consistent with an L1 dwarf because of the weak NIR constraints. The strongest constraint is in the  $z$ -band, which implies a peak luminosity of  $6 \times 10^{29}$  erg s<sup>−1</sup> for a distance of 330 pc. This is similar to the L1 flare reported by De Luca et al. (2020).

We now turn our attention to the three last SBO candidates with possible host associations: XT 050925, 160220, and 140811. These have been classified as galaxies based on morphology (Table 2) but are potentially blends of two point sources, implying that the transient would be a flare from one of the foreground stars. By comparing the optical and NIR photometry with X-ray data, we find that all three are consistent with being dwarf flares for M dwarfs at  $\sim 3$  kpc or L dwarfs at  $\sim 300$  pc. However, this would require them to be among the most luminous dwarf flares for either spectral type. Furthermore, if these sources indeed consist of two blended sources, then using the combined magnitude of the two sources as we have done above would underestimate the true X-ray flux.

Dust could, in principle, obscure the emission of an optical source. However, this is challenging to reconcile with the H column density through the Milky Way (Table 4, Willingale et al. 2013). Furthermore, the observed X-ray spectra generally indicate very low levels of optical and NIR absorption (Predehl & Schmitt 1995).

To summarize, it is possible that at least some of the bottom four candidates: XT 050925, 160220, 140811, and 040610, are dwarf flares. However, we are not able to firmly conclude this without additional data.

## 8.2. Gamma-Ray Bursts

The prompt GRB phase evolves on timescales of 0.3 s for short GRBs and 10 s for long GRBs (Meegan et al. 1996; von Kienlin et al. 2020). The spectra typically peak at energies in the range 100–1000 keV (Goldstein et al. 2012), and extend into soft X-ray energies (Villasenor et al. 2005; Lien et al. 2016). Both types are followed by afterglows with luminosities in the range  $10^{47}\text{--}10^{51}$  erg s<sup>−1</sup> at 100 s that decay on timescales of hours to days (Berger 2014; Bauer et al. 2017). The spectral shape in the 0.3–10 keV range is a power law with photon indices in the range  $\sim 1.5\text{--}3$  (Zhang et al. 2007; Racusin et al. 2009).

If the SBO candidates are related to GRBs, the peak luminosities have to be much lower than typical GRB afterglows (Figure 4 of Bauer et al. 2017). For the can-

didates with host galaxies, it is highly unlikely that the true redshifts are substantially higher than estimated. The lack of a sharply rising prompt phase, overall light curve shapes, and spectra are also difficult to reconcile with standard on-axis GRBs.

GRBs could potentially agree with some of our observations if observed far off-axis. This applies to both short (Sun et al. 2019; Xue et al. 2019; Dado & Dar 2020) and long GRBs (Dado & Dar 2019). The effects of a large viewing angle are longer duration, much lower peak luminosity, lower spectral peak, and lower fluence. The models for off-axis GRBs can be adjusted to agree qualitatively with our observations; however, many model parameters are essentially unconstrained and can be tuned to produce a very large range of observed timescales, spectra, and energies.

Another source of emission is the hot cocoon, which is the result of interactions between the jet and surrounding material. This is produced in both short (Lazzati et al. 2017) and long (Suzuki & Shigeyama 2013; De Colle et al. 2018) GRBs. The predictions for both types are X-ray transients with peak luminosities around  $10^{46}$ – $10^{48}$  erg s $^{-1}$  and fast rise times, with the details being quite sensitive to the off-axis angle. Cocoon emission from short GRBs is expected to evolve on timescales of  $< 30$  s with temperatures of 0.2–2 keV. The corresponding values for long GRBs are  $\sim 100$  s and  $\sim 0.2$  keV. We note that these values agree reasonably well with the most luminous of the observed transients, XT 030206, particularly for a long GRB cocoon.

### 8.3. Other Possibilities

There are other astrophysical sources that could give rise to X-ray transients. Many of these are expected to also produce persistent optical emission. Therefore, we note that the optical constraints discussed in Section 8.1 (Equation 8) are general and apply to any type of object, such as a companion star in an X-ray binary. It is also important to consider the Galactic latitude of the SBO candidates (Table 1). Galactic objects are generally confined to the Galactic plane, except for objects that are expected to be very close, such as late-type dwarfs. Furthermore, the prior probability of a neutron star to align with an extragalactic source is  $< 1\%$  for a neutron star solid angle density of 1000 deg $^{-2}$  (Ofek 2009; Sartore et al. 2010). Here, we very briefly mention a number of potential sources without exploring all details. We simply note that the following classes are able to produce some, but not all, of the observables without significant fine-tuning or requiring very rare circumstances.

Tidal disruption events (Rees 1988; Phinney 1989) produce soft X-ray transients that typically evolve on

timescales of 10–300 days (Komossa 2015; Kochanek 2016). This scenario involves an ordinary star being accreted onto a supermassive black hole, which also determines the timescale. This is much longer than the SBO candidates, but disruptions of white dwarfs by intermediate mass black holes have been suggested to produce tidal disruption events on timescales of  $\sim 10$  ks (Fernández et al. 2019; Shen 2019; Maguire et al. 2020).

X-ray binaries (Noorae 2013; Walter et al. 2015; Martínez-Núñez et al. 2017) can produce a number of different types of X-ray flares. Type-I (thermonuclear) X-ray bursts (Galloway & Keek 2017; Galloway et al. 2020) have peak luminosities of  $\sim 3 \times 10^{38}$  erg s $^{-1}$  and evolve on timescales of 10–300 s, but can extend up to several thousand seconds in some cases. Ordinary accretion processes and type-II outbursts (van den Eijnden et al. 2017) generally do not produce the high dynamic ranges that characterize flares. So-called supergiant fast X-ray transients (Romano 2015; Ducci et al. 2019; Sguera et al. 2020) are  $\sim 3$  ks flares with dynamic ranges of  $\sim 10^4$  and peak luminosities on the order of  $10^{37}$  erg s $^{-1}$ , which are driven by wind accretion from OB supergiant companions. Although X-ray binaries can produce a range of X-ray transients, they are necessarily associated with bright companions that are challenging to reconcile with our optical and NIR data.

White dwarf binaries (Mukai 2017) produce variable X-ray emission through accretion and surface nuclear burning (Schwarz et al. 2011; Morii et al. 2013; Starrfield et al. 2016; Ness 2019). They can produce very soft spectra and evolve on short timescales, but typically do not flare with sufficiently large dynamic ranges to be confused with SN SBOs.

Magnetars (Turolla et al. 2015; Mereghetti et al. 2015; Kaspi & Beloborodov 2017) are isolated neutron stars that are characterized by very strong magnetic fields. They are known to produce high-energy transient emission, most notably so-called giant flares (Hurley et al. 2005; Palmer et al. 2005). These are much harder than the SBO candidates and have light curves with a more prompt burst of  $\sim 1$  s followed by a much fainter decaying tail, similar to short GRBs.

## 9. SUMMARY AND CONCLUSIONS

When a star undergoes core collapse, a shock is launched from the core. This shock propagates through the star and when it reaches the surface, a burst of soft X-rays is released. This is the first electromagnetic signal that escapes a core-collapse SN and it carries independent information about the progenitor radius, asymmetries, and final mass-loss history. The X-ray transients are characterized by total energies on the order of



$10^{45}$ – $10^{47}$  erg, timescales of 10–1000 s, and soft spectra corresponding to temperatures of 0.03–3 keV. These values depend sensitively on the type of progenitor. RSGs generally produce slower and cooler SBOs, BSG SBOs are intermediate, and SBOs from WR progenitors are faster and hotter.

We search the *XMM-Newton* archive for serendipitously observed SN SBOs. This archive is likely to contain more SN SBOs than any other because of the large effective area, large FoV, and 20 year lifetime of *XMM-Newton*. Our search results in 12 SN SBO candidates. They are all consistent with being SBOs, but it is possible that a few are Galactic foreground dwarf stars or produced by other types of extragalactic sources. We focus on the SN SBO interpretation and investigate the inferred physical properties. In addition to the X-ray data, we analyze public wide-field optical and NIR data and find host galaxy candidates for nine of the sources. We estimate host redshifts of 0.1–0.6, except for one source at redshift 1.17.

The SBO candidates have energies on the order of  $10^{46}$  erg, timescales ranging from minutes to hours, and soft spectra with color temperatures of 0.1–1 keV. Using these observables, we are able to infer progenitor and SN properties. Two candidates are probably SBOs from BSGs. A third candidate is similar but slightly slower, which could be interpreted as an asymmetric BSG SBO or breakout from a wind surrounding a more compact WR progenitor (similar to SN 2008D). There is one transient with a total energy of  $8 \times 10^{47}$  erg, which is higher than SBO predictions. This could potentially be the SBO from an extreme SN. There are two more sources that are likely BSG SBOs, but lack host galaxy identifications and are more uncertain. Two candidates appear to be extreme cases of RSG or possibly yellow supergiant SBOs. Finally, the last four candidates could either be asymmetric BSG SBOs, WR wind SBOs, or Galactic foreground contamination.

Many of the SBO candidates show signs of significant asymmetries or optically thick CSM. This is consistent with both theory and other types of observations of core-collapse SNe. Asymmetries arise spontaneously during the core-collapse process and primarily affect the timescale of the SBO. We emphasize that this very naturally explains a broader diversity in SBO durations (up to 20 % of the shock crossing time) than expected from spherical models. This additional variance agrees well with our observations. The effect of CSM on the SBO candidates is more difficult to disentangle due to the very large parameter space, which can give rise to a wide range of observables. More detailed conclusions need further modeling of the individual sources, deeper

optical data, and spectroscopic redshifts. Optical follow-up data of the SNe would also ideally be obtained. This will be the subject of future studies.

Future X-ray observations will detect an ever-increasing number of SN SBOs. The X-ray instrument currently most likely to detect SBOs is *eROSITA* (Predehl et al. 2010; Predehl 2017). We predict *eROSITA* to detect 2 SN SBOs per year using Equations 43 of Sapir et al. (2013) and 97 of Waxman & Katz (2017). This is a back-of-the-envelope estimate where we also attempt to correct for ISM absorption and the diversity in observed properties. We conclude by emphasizing the importance of live analyses of future X-ray data and rapid follow-up observations to fully capitalize on these rare opportunities.

## ACKNOWLEDGMENTS

We are grateful to Annap Wongwathanarat for providing measures of SBO asymmetries from SN simulations, and Eleni Tsaprazi for large-scale structure density contrasts. We also thank Claes Fransson and Jens Jasche for helpful discussions, and the anonymous referee for the comments. This work was supported by the Knut and Alice Wallenberg Foundation. This research has made use of data obtained from the 3XMM *XMM-Newton* serendipitous source catalogue compiled by the 10 institutes of the *XMM-Newton* Survey Science Centre selected by ESA. This research has made use of data produced by the EXTraS project, funded by the European Union’s Seventh Framework Programme under grant agreement no 607452. This research has made use of data obtained through the High Energy Astrophysics Science Archive Research Center Online Service, provided by the NASA/Goddard Space Flight Center. This research has made use of the SIMBAD database, operated at CDS, Strasbourg, France. This research has made use of the VizieR catalogue access tool, CDS, Strasbourg, France. This research has made use of “Aladin sky atlas” developed at CDS, Strasbourg Observatory, France. This research made use of *hips2fits*<sup>9</sup>, a service provided by CDS. This research has made use of NASA’s Astrophysics Data System.

*Facilities:* XMM (EPIC)

*Software:* ADS (Kurtz et al. 2000), Aladin (Bonnarel et al. 2000; Boch & Fernique 2014), astropy (3.0.4; Astropy Collaboration et al. 2013, 2018),

<sup>9</sup> <https://alasky.u-strasbg.fr/hips-image-services/hips2fits>

FTOOLS (Blackburn 1995), HEASoft (6.26.1; Nasa High Energy Astrophysics Science Archive Research Center (Heasarc) 2014), Le PHARE (2.2; Arnouts et al. 1999; Ilbert et al. 2006), matplotlib (2.0.2; Hunter 2007), numpy

(1.13.1; van der Walt et al. 2011), SAOImage DS9 (8.1; Joye & Mandel 2003), SAS (18.0.0; Gabriel et al. 2004), scipy (1.1.0; Virtanen et al. 2020). SIMBAD (Wenger et al. 2000), VizieR (Ochsenbeim et al. 2000), XSPEC (12.10.1f; Arnaud 1996).

## APPENDIX

### A. SEARCHING THE *XMM-Newton* OBSERVATIONS

We use two different algorithms to search for SN SBOs in archival *XMM-Newton* data. The aim of both search algorithms is solely to identify X-ray transients. Rejecting spurious detections and careful source identification is performed in a subsequent stage (Section 2.2). For these reasons, we do not attempt to correct for instrumental effects such as vignetting, deadtime, or chip gaps in the transient detection process. Some details related to data preparation are also not considered, such as extraction regions falling outside of CCDs and nearby sources located within background regions. These effects are managed in the proper data reduction (Section 4) for the final SBO candidates.

Notably, we do not exclude periods of high background when searching for transients because transients can occur during these times and could, in principle, be securely identified. The high background is produced by protons in the Earth’s magnetosphere and depends on the satellite altitude and level of solar activity (Carter & Read 2007). These proton flares affect 30 to 40 % of the total *XMM-Newton* observation time. Excluding these time periods increases the S/N of typical persistent sources, but this is not true for a transient source that is only detectable during a background flare. The challenge is to distinguish an interesting astrophysical transient from background flares. This distinction is difficult to do solely using light curves, but can easily be done in images because background flares affect the CCDs uniformly whereas a transient source appears as a point.

#### A.1. Custom Transient Source Finder

Our custom algorithm starts from the Processing Pipeline Subsystem (PPS) event lists and finds all variable sources. We use all 11,500 public observations with EPIC imaging archived at HEASARC as of 2019 November 11. Since we are expecting faint and soft sources, we combine the data from all EPIC cameras (Strüder et al. 2001; Turner et al. 2001) and restrict the energy range to 0.3–2 keV.

The first step of the search algorithm is to bin the event list along the spatial and temporal dimensions. Effectively, this creates a series of images (a data cube) for each observation, which is divided into three-dimensional “cells” with two spatial and one temporal dimension. The spatial binning is  $20 \times 20$  arcsec<sup>2</sup>, which is chosen to contain the cores of the PSFs of EPIC. The encircled energy at a radius of 10 arcsec is around 60 % for EPIC. The PSF wings are much broader and can be neglected. The temporal binning is performed at 5 different timescales ranging from 100 s to 10,000 s with logarithmic spacing. To mitigate the effects of the discretizations in space and time, we repeat the binning by shifting the grid by half the bin size along each dimension. The total number of combinations introduced by the shifts and temporal binning at different timescales is 40 ( $2 \times 2 \times 2 \times 5$ ). This means that 40 data cubes are created for each observation.

The second step is to find transients in the data cubes. To do this, we perform a simplified statistical test for variability in each cell relative to the grid cells before and after. Before and after in this context refers to the cells at the same spatial position, but one bin earlier and later along the temporal dimension, respectively. Importantly, the transient detection algorithm must be able to handle the highly temporally varying background and reject slowly varying sources. For each cell, we first need to estimate the expected persistent source flux at the position. This is done by linearly interpolating the background-subtracted fluxes of the cells before and after in time. The background subtraction in the before and after cells are performed by subtracting the average of the four spatially neighboring grid cells at the respective times. To prevent over-subtraction (negative counts), we simply force the expected source flux in the current bin to be at least 1 count. This provides the expected persistent source flux at the current position. To this flux, we add the average background of the four spatially neighboring pixels. This sum is the expected total count rate in the current cell. Finally, we assume the count rate to be Poissonian and compute the  $p$ -value to obtain the

observed count rate given the expected rate. This  $p$ -value should capture any variability in excess of linear variability in time, while also being insensitive to the highly temporally varying background.

To separate the variable sources, we perform a cut based on the variability measure. As a test statistic, we rescale the  $p$ -value and use the negative log-likelihood  $-\ln(p)$ . We select a limiting statistic of 25, which leaves a very low probability of noise passing the filter. This cut leaves 380 detections, which are investigated by eye in subsequent steps.

#### A.2. Finding Transients in 3XMM-DR8

The *XMM-Newton* Survey Science Centre routinely publishes catalogs of detected sources, the latest being 3XMM-DR8 at the time of writing. This catalog contains observations from 2000 February 3 through 2017 November 30 and contains 775,153 detections of 531,454 unique sources. The first step toward identifying SBOs is analyzing the source light curves. 3XMM-DR8 includes light curves, but those are not suited for fast transients because they were created with a common bin-width with a minimum number of photons in every bin (Section 5.2 of [Watson et al. 2009](#)). Consequently, the time interval before the rise of a transient source (and possibly also after the transient has faded) results in an increased common bin-width. This increase could drastically reduce the sensitivity for short, bright flare-like transients. For these reasons, we decide to construct custom light curves for our SBO search.<sup>10</sup>

We use the positions from the 3XMM-DR8 catalog of identified sources and generate light curves for all 550,614 detections that are more than  $15^\circ$  outside of the Galactic plane. We do not search the Galactic plane because we found no candidates in this region using our custom finder and because robust source identification is very difficult in dense fields. The increased X-ray absorption close to the Galactic plane also drastically reduces the possibility of detecting SBOs. Furthermore, we discard very faint sources by omitting all objects with a detection likelihood reported by 3XMM-DR8 as less than 10. This likelihood is based on the likelihood ratio described by [Cash \(1979\)](#). The likelihood is defined as  $-\ln(P)$ , where  $P$  is the probability of the detection occurring by chance (formally, the probability of the null hypothesis; Section 4.4.3 of [Watson et al. 2009](#)).

To create the light curves, we download the *XMM-Newton* PPS event lists and combine all exposures of the EPIC pn, MOS1, and MOS2 cameras within each observation and limit the energy range to 0.3–10 keV. From the combined event list, we extract source events from a circular region with a radius of 20 arcsec centered on the source position (taken from 3XMM-DR8). Background events are then extracted from an annular region centered on the source with an inner radius 50 arcsec and an outer radius of 100 arcsec. The light curves are binned such that each bin contains 25 counts from the source region. This binning requirement ignores the background count rate and results in bins with different temporal widths. The reason for choosing this dynamic-binning approach is to be able to effectively capture the large variations in flux for transient sources. The background events are binned to the same temporal bins as the source light curves and are then subtracted from the source to create a final light curve.

The next step is to find all transient sources. We identify sources showing transient-like behavior by requiring that they fulfill at least one of the following heuristics:

- The ratio of the maximum background-subtracted flux bin over the 50th flux percentile (i.e. percentile of the bins weighted by time for this individual light curve) is larger than 3, while the signal-to-background ratio (S/B) is higher than 10 at the time of peak flux.
- Same as above, but with a peak flux a factor of 5 above the 50th percentile and a S/B of at least 3.
- At least 10 ks of the background-subtracted light curve is within  $1\sigma$  of 0 counts  $\text{s}^{-1}$ . Moreover, at least one bin has a source flux higher than 0.05 counts  $\text{s}^{-1}$  with a S/B higher than 3.

The combination of all heuristics is constructed to distinguish flare-like sources while being insensitive to background flares and inaccurate background subtraction. All heuristics are then also re-evaluated with the modification that the

<sup>10</sup> We note that the Exploring the X-ray Transient and variable Sky (EXTraS) project ([De Luca et al. 2016](#)) aim to provide more detailed temporal data products for all *XMM-Newton* sources. However, the EXTraS data for aperiodic short-term variability (EXTraS Working Package 2) only includes data that were publicly available by 2012 December 31 (corresponding to 3XMM-DR4). The EXTraS light curves are also intended for general variable behavior and are not optimized for fast and possibly faint transients. For these reasons, we only briefly inspected the EXTraS WP2 catalog, and we find no objects that were not already detected by our other methods.

time intervals when the background count rate is higher than  $0.05 \text{ counts s}^{-1}$  are discarded.<sup>11</sup> Approximately 11,000 sources pass these criteria and are investigated by eye at a subsequent stage. This can be compared to 3XMM-DR8, which classifies 5934 sources as variable. The difference in the number of variable sources is not surprising because of our simplified background treatment, which results in a very large number of sources being classified as variable due to inaccurately subtracted background flares. Furthermore, these numbers are not strictly comparable because we apply a number of filters and have defined variability differently.

## B. HOST PHOTOMETRY

Table B.1 provides the optical and NIR data for the candidate host galaxies. The multi-band optical data are used for the redshift SED fitting. Specifically, we only use optical data from a single survey for each source to avoid systematic uncertainties between different surveys. It is not possible to perform reliable SED fits using only NIR data, but the NIR data are still useful since they provide an important check for the inferred absolute magnitudes.

## C. FIT STATISTICS

Table C.1 provides statistic measures for all spectral fits. We note that the number of photons (essentially the degrees of freedom) is very limited in some cases, especially for the time-resolved spectra. This introduces substantial variance in the goodness measures.

<sup>11</sup> We note that the limit of  $0.05 \text{ counts s}^{-1}$  refers to the rate of our custom background light curves. These light curves are different from the background light curves in the standard *XMM-Newton* data reduction, which are customarily defined as the total rate in the entire FoV within 10–12 keV for the pn CCD and above 10 keV for the MOS CCDs.



Table B.1. Host Photometry

XT	$m_u$ (mag <sub>AB</sub> )	$m_g$ (mag <sub>AB</sub> )	$m_r$ (mag <sub>AB</sub> )	$m_i$ (mag <sub>AB</sub> )	$m_z$ (mag <sub>AB</sub> )	$m_Y$ (mag <sub>AB</sub> )	$m_J$ (mag <sub>AB</sub> )	$m_H$ (mag <sub>AB</sub> )	$m_K$ (mag <sub>AB</sub> )	Source
161028	$22.2 \pm 0.3$	$21.46 \pm 0.32$	$20.69 \pm 0.06$	$20.50 \pm 0.10$	$20.40 \pm 0.29$	...	$> 18.01$	$> 17.79$	$> 17.15$	SDSS16/2MASS
151219	$23.1 \pm 0.2$	$22.37 \pm 0.05$	$21.49 \pm 0.02$	$20.88 \pm 0.06$	$20.94 \pm 0.20$	$20.68 \pm 0.30$	$20.57 \pm 0.35$	$20.3 \pm 0.3$	$19.6 \pm 0.2$	KIDS/VIKING
110621	...	$19.68 \pm 0.01$	$19.63 \pm 0.01$	$19.34 \pm 0.01$	$19.39 \pm 0.02$	$19.38 \pm 0.07$	$19.17 \pm 0.13$	...	$19.9 \pm 0.3$	DES/VHS
030206	...	$21.89 \pm 0.11$	$22.05 \pm 0.12$	$22.37 \pm 0.11$	$21.73 \pm 0.15$	$> 21.3$	$> 18.01$	$> 17.79$	$> 17.15$	Pan-STARRS/2MASS
070618	...	$> 24.3$	$> 24.08$	$> 23.44$	$> 22.69$	$> 21.44$	$> 18.01$	$> 17.79$	$> 17.15$	DES/2MASS
060207	$> 17.9$	$> 18.0$	$> 18.0$	$> 18.0$	$> 18.0$	...	$> 21.11$	...	$> 19.95$	SkyMapper/VHS
100424	...	$21.4 \pm 0.06$	$20.37 \pm 0.04$	$19.97 \pm 0.02$	$19.73 \pm 0.03$	$19.33 \pm 0.07$	$> 18.01$	$> 17.79$	$> 17.15$	Pan-STARRS/2MASS
151128	...	$21.5 \pm 0.10$	$20.30 \pm 0.04$	$19.83 \pm 0.03$	$19.47 \pm 0.03$	$19.63 \pm 0.09$	$> 18.01$	$> 17.79$	$> 17.15$	Pan-STARRS/2MASS
050925	$> 17.9$	$> 18.0$	$> 18.0$	$> 18.0$	$> 18.0$	$21.53 \pm 0.57$	$20.69 \pm 0.51$	...	$> 20.35$	SkyMapper/VHS
160220	$> 17.9$	$> 18.0$	$> 18.0$	$> 18.0$	$> 18.0$	...	$20.25 \pm 0.28$	$> 17.79$	$> 17.15$	SkyMapper/VHS
140811	...	$21.80 \pm 0.06$	$20.61 \pm 0.02$	$19.71 \pm 0.01$	$19.32 \pm 0.02$	$19.02 \pm 0.04$	$> 18.01$	$> 17.79$	$> 17.15$	Pan-STARRS/2MASS
040610	...	$> 22.9$	$> 22.8$	$> 22.7$	$> 21.9$	$> 20.9$	$> 18.01$	$> 17.79$	$> 17.15$	Pan-STARRS/2MASS

NOTE—All magnitudes are converted (Hewett et al. 2006; Blanton & Roweis 2007) to the AB magnitude system (Oke & Gunn 1983). All detections use either Petrosian (1976) or Kron (1980) magnitudes, which are suitable for extended sources. We note that the upper limits are given for different thresholds:  $3\sigma$  (2MASS),  $5\sigma$  (Pan-STARRS and VHS), S/N of 10 (DES), and  $10\sigma$  (SkyMapper). The limits are for point sources except for the DES limits, which are for apertures of 1.95 arcsec. For reference, Metcalfe et al. (2013) find that galaxies have a 50% completeness about 0.4 mag<sub>AB</sub> brighter than stars using Pan-STARRS observations. Filters of different telescopes are also slightly different.

**References**—Sloan Digital Sky Survey Data Release 16 (SDSS-IV DR16, York et al. 2000; Ahumada et al. 2019), Two Micron All Sky Survey (2MASS, Skrutskie et al. 2006), Kilo-Degree Survey Data Release 3 (KiDS-ESO-DR3, de Jong et al. 2013, 2017), Visible and Infrared Survey Telescope for Astronomy (VISTA) Kilo-degree Infrared Galaxy Survey Data Release 2 (VIKING DR2, Edge et al. 2013), Dark Energy Survey Data Release 1 (DES DR1, Abbott et al. 2018), VISTA Hemisphere Survey Data Release 4.1 (VHS DR4.1, McMahon et al. 2013), Panoramic Survey Telescope and Rapid Response System Data Release 2 (Pan-STARRS DR2, Chambers et al. 2016), SkyMapper (Wolf et al. 2018).

Table C.1. Fitting Statistics

XT	$C_{\text{BB}}/\text{DoF}$	$G_{\text{BB}}$	$C_{\text{BB},1}/\text{DoF}$	$G_{\text{BB},1}$	$C_{\text{BB},2}/\text{DoF}$	$G_{\text{BB},2}$	$C_{\text{PL}}/\text{DoF}$	$G_{\text{PL}}$	$C_{\text{PL},1}/\text{DoF}$	$G_{\text{PL},1}$	$C_{\text{PL},2}/\text{DoF}$	$G_{\text{PL},2}$
161028	44/43 = 1.02	0.82	18/20 = 0.92	0.59	29/19 = 1.55	0.98	41/43 = 0.95	0.66	17/20 = 0.86	0.47	30/19 = 1.55	0.98
151219	71/64 = 1.11	0.94	43/31 = 1.39	0.97	35/32 = 1.10	0.83	66/64 = 1.03	0.81	41/31 = 1.31	0.89	33/32 = 1.04	0.71
110621	55/53 = 1.04	0.61	17/24 = 0.70	0.09	32/25 = 1.29	0.78	56/53 = 1.05	0.62	17/24 = 0.72	0.10	32/25 = 1.29	0.79
030206	187/209 = 0.89	0.96	123/133 = 0.93	0.95	103/93 = 1.11	0.99	169/209 = 0.81	0.58	118/133 = 0.88	0.87	99/93 = 1.07	0.96
070618	141/177 = 0.80	0.88	84/106 = 0.79	0.81	61/74 = 0.82	0.76	128/177 = 0.72	0.45	77/106 = 0.73	0.43	60/74 = 0.81	0.69
060207	42/48 = 0.88	0.47	23/24 = 0.97	0.54	11/20 = 0.57	0.18	39/48 = 0.81	0.31	23/24 = 0.96	0.48	10/20 = 0.51	0.09
100424	80/80 = 1.01	0.69	36/41 = 0.89	0.39	42/42 = 1.00	0.52	75/80 = 0.94	0.33	36/41 = 0.89	0.26	36/42 = 0.86	0.19
151128	51/34 = 1.50	1.00	29/19 = 1.52	0.98	17/11 = 1.55	0.96	45/34 = 1.32	0.90	28/19 = 1.49	0.78	15/11 = 1.39	0.87
050925	40/32 = 1.24	0.81	28/20 = 1.41	0.90	10/9 = 1.12	0.48	35/32 = 1.08	0.50	24/20 = 1.19	0.64	8/9 = 0.94	0.33
160220	82/83 = 0.99	0.56	43/40 = 1.09	0.69	30/41 = 0.73	0.09	76/83 = 0.92	0.27	39/40 = 0.96	0.34	30/41 = 0.74	0.07
140811	108/88 = 1.23	0.99	24/24 = 1.00	0.67	64/62 = 1.03	0.82	101/88 = 1.15	0.83	22/24 = 0.93	0.39	63/62 = 1.02	0.56
040610	117/141 = 0.83	0.30	26/37 = 0.70	0.15	101/102 = 0.99	0.66	110/141 = 0.78	0.07	18/37 = 0.50	0.02	102/102 = 1.00	0.55

NOTE—Quantities denoted by  $C$  are fit statistics and  $G$  are goodness measures (Section 5.1). The subscripts are BB for blackbody and PL for power law, and first (1) and second (2) interval for time-resolved spectra. Quantities without subscript integers are time-integrated values. DoF refers to the degrees of freedom.

## REFERENCES

- Abbott, T. M. C., Abdalla, F. B., Allam, S., et al. 2018, *ApJS*, 239, 18, doi: [10.3847/1538-4365/aae9f0](https://doi.org/10.3847/1538-4365/aae9f0)
- Abellán, F. J., Indebetouw, R., Marcaide, J. M., et al. 2017, *ApJL*, 842, L24, doi: [10.3847/2041-8213/aa784c](https://doi.org/10.3847/2041-8213/aa784c)
- Ahumada, R., Allende Prieto, C., Almeida, A., et al. 2019, arXiv e-prints, arXiv:1912.02905, <https://arxiv.org/abs/1912.02905>
- Alam, S., Albareti, F. D., Allende Prieto, C., et al. 2015, *ApJS*, 219, 12, doi: [10.1088/0067-0049/219/1/12](https://doi.org/10.1088/0067-0049/219/1/12)
- Alp, D., Larsson, J., Maeda, K., et al. 2019, *ApJ*, 882, 22, doi: [10.3847/1538-4357/ab3395](https://doi.org/10.3847/1538-4357/ab3395)
- Arnaud, K. A. 1996, in *Astronomical Society of the Pacific Conference Series*, Vol. 101, *Astronomical Data Analysis Software and Systems V*, ed. G. H. Jacoby & J. Barnes, 17
- Arnouts, S., Cristiani, S., Moscardini, L., et al. 1999, *MNRAS*, 310, 540, doi: [10.1046/j.1365-8711.1999.02978.x](https://doi.org/10.1046/j.1365-8711.1999.02978.x)
- Arnouts, S., Walcher, C. J., Le Fèvre, O., et al. 2007, *A&A*, 476, 137, doi: [10.1051/0004-6361:20077632](https://doi.org/10.1051/0004-6361:20077632)
- Astropy Collaboration, Robitaille, T. P., Tollerud, E. J., et al. 2013, *A&A*, 558, A33, doi: [10.1051/0004-6361/201322068](https://doi.org/10.1051/0004-6361/201322068)
- Astropy Collaboration, Price-Whelan, A. M., Sipőcz, B. M., et al. 2018, *AJ*, 156, 123, doi: [10.3847/1538-3881/aabc4f](https://doi.org/10.3847/1538-3881/aabc4f)
- Avni, Y. 1976, *ApJ*, 210, 642, doi: [10.1086/154870](https://doi.org/10.1086/154870)
- Balberg, S., & Loeb, A. 2011, *Monthly Notices of the Royal Astronomical Society*, 414, 1715, doi: [10.1111/j.1365-2966.2011.18505.x](https://doi.org/10.1111/j.1365-2966.2011.18505.x)
- Barthelmy, S. D., Barbier, L. M., Cummings, J. R., et al. 2005, *SSRv*, 120, 143, doi: [10.1007/s11214-005-5096-3](https://doi.org/10.1007/s11214-005-5096-3)
- Bauer, F. E., Treister, E., Schawinski, K., et al. 2017, *MNRAS*, 467, 4841, doi: [10.1093/mnras/stx417](https://doi.org/10.1093/mnras/stx417)
- Benz, A. O., & Güdel, M. 2010, *ARA&A*, 48, 241, doi: [10.1146/annurev-astro-082708-101757](https://doi.org/10.1146/annurev-astro-082708-101757)
- Berger, E. 2014, *ARA&A*, 52, 43, doi: [10.1146/annurev-astro-081913-035926](https://doi.org/10.1146/annurev-astro-081913-035926)
- Blackburn, J. K. 1995, in *Astronomical Society of the Pacific Conference Series*, Vol. 77, *Astronomical Data Analysis Software and Systems IV*, ed. R. A. Shaw, H. E. Payne, & J. J. E. Hayes, 367
- Blanton, M. R., & Roweis, S. 2007, *AJ*, 133, 734, doi: [10.1086/510127](https://doi.org/10.1086/510127)
- Blanton, M. R., Hogg, D. W., Bahcall, N. A., et al. 2003, *ApJ*, 592, 819, doi: [10.1086/375776](https://doi.org/10.1086/375776)
- Blinnikov, S., Lundqvist, P., Bartunov, O., Nomoto, K., & Iwamoto, K. 2000, *ApJ*, 532, 1132, doi: [10.1086/308588](https://doi.org/10.1086/308588)
- Boch, T., & Fernique, P. 2014, in *Astronomical Society of the Pacific Conference Series*, Vol. 485, *Astronomical Data Analysis Software and Systems XXIII*, ed. N. Manset & P. Forshay, 277
- Bochanski, J. J., Hawley, S. L., & West, A. A. 2011, *AJ*, 141, 98, doi: [10.1088/0004-6256/141/3/98](https://doi.org/10.1088/0004-6256/141/3/98)
- Bonnarel, F., Fernique, P., Bienaymé, O., et al. 2000, *A&AS*, 143, 33, doi: [10.1051/aas:2000331](https://doi.org/10.1051/aas:2000331)
- Bruzual, G., & Charlot, S. 2003, *MNRAS*, 344, 1000, doi: [10.1046/j.1365-8711.2003.06897.x](https://doi.org/10.1046/j.1365-8711.2003.06897.x)
- Caballero-García, M. D., Šimon, V., Jelínek, M., et al. 2015, *MNRAS*, 452, 4195, doi: [10.1093/mnras/stv1565](https://doi.org/10.1093/mnras/stv1565)
- Calzavara, A. J., & Matzner, C. D. 2004, *Monthly Notices of the Royal Astronomical Society*, 351, 694, doi: [10.1111/j.1365-2966.2004.07818.x](https://doi.org/10.1111/j.1365-2966.2004.07818.x)
- Calzetti, D., Kinney, A. L., & Storchi-Bergmann, T. 1994, *ApJ*, 429, 582, doi: [10.1086/174346](https://doi.org/10.1086/174346)
- Carnero Rosell, A., Santiago, B., dal Ponte, M., et al. 2019, *MNRAS*, 489, 5301, doi: [10.1093/mnras/stz2398](https://doi.org/10.1093/mnras/stz2398)
- Carter, J. A., & Read, A. M. 2007, *A&A*, 464, 1155, doi: [10.1051/0004-6361:20065882](https://doi.org/10.1051/0004-6361:20065882)
- Cash, W. 1976, *A&A*, 52, 307
- . 1979, *ApJ*, 228, 939, doi: [10.1086/156922](https://doi.org/10.1086/156922)
- Chambers, K. C., Magnier, E. A., Metcalfe, N., et al. 2016, arXiv e-prints, arXiv:1612.05560, <https://arxiv.org/abs/1612.05560>
- Chevalier, R. A., & Fransson, C. 2008, *ApJL*, 683, L135, doi: [10.1086/591522](https://doi.org/10.1086/591522)
- Coleman, G. D., Wu, C. C., & Weedman, D. W. 1980, *ApJS*, 43, 393, doi: [10.1086/190674](https://doi.org/10.1086/190674)
- Cook, B. A., Williams, P. K. G., & Berger, E. 2014, *ApJ*, 785, 10, doi: [10.1088/0004-637X/785/1/10](https://doi.org/10.1088/0004-637X/785/1/10)
- Couch, S. M. 2017, *Philosophical Transactions of the Royal Society of London Series A*, 375, 20160271, doi: [10.1098/rsta.2016.0271](https://doi.org/10.1098/rsta.2016.0271)
- Couch, S. M., Pooley, D., Wheeler, J. C., & Milosavljević, M. 2011, *ApJ*, 727, 104, doi: [10.1088/0004-637X/727/2/104](https://doi.org/10.1088/0004-637X/727/2/104)
- Dado, S., & Dar, A. 2019, *ApJL*, 884, L44, doi: [10.3847/2041-8213/ab499b](https://doi.org/10.3847/2041-8213/ab499b)
- . 2020, *PhRvD*, 101, 063008, doi: [10.1103/PhysRevD.101.063008](https://doi.org/10.1103/PhysRevD.101.063008)
- Dalya, G., Frei, Z., Galgoczi, G., Raffai, P., & de Souza, R. S. 2016, *VizieR Online Data Catalog*, VII/275
- De Colle, F., Lu, W., Kumar, P., Ramirez-Ruiz, E., & Smoot, G. 2018, *MNRAS*, 478, 4553, doi: [10.1093/mnras/sty1282](https://doi.org/10.1093/mnras/sty1282)

- de Jong, J. T. A., Verdoes Kleijn, G. A., Kuijken, K. H., & Valentijn, E. A. 2013, *Experimental Astronomy*, 35, 25, doi: [10.1007/s10686-012-9306-1](https://doi.org/10.1007/s10686-012-9306-1)
- de Jong, J. T. A., Verdoes Kleijn, G. A., Erben, T., et al. 2017, *A&A*, 604, A134, doi: [10.1051/0004-6361/201730747](https://doi.org/10.1051/0004-6361/201730747)
- De Luca, A., Salvaterra, R., Tiengo, A., et al. 2016, *The Universe of Digital Sky Surveys*, 42, 291, doi: [10.1007/978-3-319-19330-4\\_46](https://doi.org/10.1007/978-3-319-19330-4_46)
- De Luca, A., Stelzer, B., Burgasser, A. J., et al. 2020, *A&A*, 634, L13, doi: [10.1051/0004-6361/201937163](https://doi.org/10.1051/0004-6361/201937163)
- Ducci, L., Romano, P., Ji, L., & Santangelo, A. 2019, *A&A*, 631, A135, doi: [10.1051/0004-6361/201936544](https://doi.org/10.1051/0004-6361/201936544)
- Edge, A., Sutherland, W., Kuijken, K., et al. 2013, *The Messenger*, 154, 32
- Ensmann, L., & Burrows, A. 1992, *ApJ*, 393, 742, doi: [10.1086/171542](https://doi.org/10.1086/171542)
- Ergon, M., Sollerman, J., Fraser, M., et al. 2014, *A&A*, 562, A17, doi: [10.1051/0004-6361/201321850](https://doi.org/10.1051/0004-6361/201321850)
- Favata, F., Reale, F., Micela, G., et al. 2000, *A&A*, 353, 987. <https://arxiv.org/abs/astro-ph/9909491>
- Fernández, R., Margalit, B., & Metzger, B. D. 2019, *MNRAS*, 488, 259, doi: [10.1093/mnras/stz1701](https://doi.org/10.1093/mnras/stz1701)
- Gabriel, C., Denby, M., Fyfe, D. J., et al. 2004, in *Astronomical Society of the Pacific Conference Series*, Vol. 314, *Astronomical Data Analysis Software and Systems (ADASS) XIII*, ed. F. Ochsenbein, M. G. Allen, & D. Egret, 759
- Gaia Collaboration, Brown, A. G. A., Vallenari, A., et al. 2018, *A&A*, 616, A1, doi: [10.1051/0004-6361/201833051](https://doi.org/10.1051/0004-6361/201833051)
- Galloway, D. K., & Keek, L. 2017, arXiv e-prints, arXiv:1712.06227. <https://arxiv.org/abs/1712.06227>
- Galloway, D. K., in 't Zand, J. J. M., Chenevez, J., et al. 2020, arXiv e-prints, arXiv:2003.00685. <https://arxiv.org/abs/2003.00685>
- Glennie, A., Jonker, P. G., Fender, R. P., Nagayama, T., & Pretorius, M. L. 2015, *MNRAS*, 450, 3765, doi: [10.1093/mnras/stv801](https://doi.org/10.1093/mnras/stv801)
- Goldstein, A., Burgess, J. M., Preece, R. D., et al. 2012, *ApJS*, 199, 19, doi: [10.1088/0067-0049/199/1/19](https://doi.org/10.1088/0067-0049/199/1/19)
- Grefenstette, B. W., Fryer, C. L., Harrison, F. A., et al. 2017, *ApJ*, 834, 19, doi: [10.3847/1538-4357/834/1/19](https://doi.org/10.3847/1538-4357/834/1/19)
- Greiner, J., Hartmann, D. H., Voges, W., et al. 2000, *Astronomy and Astrophysics*, 353, 998. <https://arxiv.org/abs/astro-ph/9910300>
- Güdel, M. 2004, *A&A Rv*, 12, 71, doi: [10.1007/s00159-004-0023-2](https://doi.org/10.1007/s00159-004-0023-2)
- Güdel, M., & Nazé, Y. 2009, *A&A Rv*, 17, 309, doi: [10.1007/s00159-009-0022-4](https://doi.org/10.1007/s00159-009-0022-4)
- Hewett, P. C., Warren, S. J., Leggett, S. K., & Hodgkin, S. T. 2006, *MNRAS*, 367, 454, doi: [10.1111/j.1365-2966.2005.09969.x](https://doi.org/10.1111/j.1365-2966.2005.09969.x)
- Hunter, J. D. 2007, *Computing in Science and Engineering*, 9, 90, doi: [10.1109/MCSE.2007.55](https://doi.org/10.1109/MCSE.2007.55)
- Hurley, K., Boggs, S. E., Smith, D. M., et al. 2005, *Nature*, 434, 1098, doi: [10.1038/nature03519](https://doi.org/10.1038/nature03519)
- Ilbert, O., Tresse, L., Zucca, E., et al. 2005, *A&A*, 439, 863, doi: [10.1051/0004-6361:20041961](https://doi.org/10.1051/0004-6361:20041961)
- Ilbert, O., Arnouts, S., McCracken, H. J., et al. 2006, *A&A*, 457, 841, doi: [10.1051/0004-6361:20065138](https://doi.org/10.1051/0004-6361:20065138)
- Ilbert, O., Capak, P., Salvato, M., et al. 2009, *ApJ*, 690, 1236, doi: [10.1088/0004-637X/690/2/1236](https://doi.org/10.1088/0004-637X/690/2/1236)
- Ito, H., Levinson, A., & Nagataki, S. 2020, *MNRAS*, 492, 1902, doi: [10.1093/mnras/stz3591](https://doi.org/10.1093/mnras/stz3591)
- Janka, H.-T., Melson, T., & Summa, A. 2016, *Annual Review of Nuclear and Particle Science*, 66, 341, doi: [10.1146/annurev-nucl-102115-044747](https://doi.org/10.1146/annurev-nucl-102115-044747)
- Jansen, F., Lumb, D., Altieri, B., et al. 2001, *A&A*, 365, L1, doi: [10.1051/0004-6361:20000036](https://doi.org/10.1051/0004-6361:20000036)
- Jones, D. H., Read, M. A., Saunders, W., et al. 2009, *MNRAS*, 399, 683, doi: [10.1111/j.1365-2966.2009.15338.x](https://doi.org/10.1111/j.1365-2966.2009.15338.x)
- Jonker, P. G., Glennie, A., Heida, M., et al. 2013, *ApJ*, 779, 14, doi: [10.1088/0004-637X/779/1/14](https://doi.org/10.1088/0004-637X/779/1/14)
- Joye, W. A., & Mandel, E. 2003, in *Astronomical Society of the Pacific Conference Series*, Vol. 295, *Astronomical Data Analysis Software and Systems XII*, ed. H. E. Payne, R. I. Jedrzejewski, & R. N. Hook, 489
- Kaspi, V. M., & Beloborodov, A. M. 2017, *Annual Review of Astronomy and Astrophysics*, 55, 261, doi: [10.1146/annurev-astro-081915-023329](https://doi.org/10.1146/annurev-astro-081915-023329)
- Katz, B., Budnik, R., & Waxman, E. 2010, *ApJ*, 716, 781, doi: [10.1088/0004-637X/716/1/781](https://doi.org/10.1088/0004-637X/716/1/781)
- Katz, B., Sapir, N., & Waxman, E. 2012, *ApJ*, 747, 147, doi: [10.1088/0004-637X/747/2/147](https://doi.org/10.1088/0004-637X/747/2/147)
- Kinney, A. L., Calzetti, D., Bohlin, R. C., et al. 1996, *ApJ*, 467, 38, doi: [10.1086/177583](https://doi.org/10.1086/177583)
- Klein, R. I., & Chevalier, R. A. 1978, *ApJL*, 223, L109, doi: [10.1086/182740](https://doi.org/10.1086/182740)
- Kochanek, C. S. 2016, *MNRAS*, 461, 371, doi: [10.1093/mnras/stw1290](https://doi.org/10.1093/mnras/stw1290)
- Komossa, S. 2015, *Journal of High Energy Astrophysics*, 7, 148, doi: [10.1016/j.jheap.2015.04.006](https://doi.org/10.1016/j.jheap.2015.04.006)
- Kron, R. G. 1980, *ApJS*, 43, 305, doi: [10.1086/190669](https://doi.org/10.1086/190669)
- Kuijken, K., Heymans, C., Dvornik, A., et al. 2019, *A&A*, 625, A2, doi: [10.1051/0004-6361/201834918](https://doi.org/10.1051/0004-6361/201834918)
- Kurtz, M. J., Eichhorn, G., Accomazzi, A., et al. 2000, *A&AS*, 143, 41, doi: [10.1051/aas:2000170](https://doi.org/10.1051/aas:2000170)
- Lampton, M., Margon, B., & Bowyer, S. 1976, *ApJ*, 208, 177, doi: [10.1086/154592](https://doi.org/10.1086/154592)



- Larsson, J., Fransson, C., Spyromilio, J., et al. 2016, *ApJ*, 833, 147, doi: [10.3847/1538-4357/833/2/147](https://doi.org/10.3847/1538-4357/833/2/147)
- Lavaux, G., Jasche, J., & Leclercq, F. 2019, arXiv e-prints, arXiv:1909.06396. <https://arxiv.org/abs/1909.06396>
- Lazzati, D., López-Cámara, D., Cantiello, M., et al. 2017, *ApJL*, 848, L6, doi: [10.3847/2041-8213/aa8f3d](https://doi.org/10.3847/2041-8213/aa8f3d)
- Levinson, A., & Nakar, E. 2019, arXiv e-prints, arXiv:1909.10288. <https://arxiv.org/abs/1909.10288>
- Lien, A., Sakamoto, T., Barthelmy, S. D., et al. 2016, *ApJ*, 829, 7, doi: [10.3847/0004-637X/829/1/7](https://doi.org/10.3847/0004-637X/829/1/7)
- Lloyd, R. O. P., Shkolnik, E. L., Schneider, A. C., et al. 2018a, *ApJ*, 867, 70, doi: [10.3847/1538-4357/aae2ae](https://doi.org/10.3847/1538-4357/aae2ae)
- Lloyd, R. O. P., France, K., Youngblood, A., et al. 2018b, *ApJ*, 867, 71, doi: [10.3847/1538-4357/aae2bd](https://doi.org/10.3847/1538-4357/aae2bd)
- Madsen, K. K., Beardmore, A. P., Forster, K., et al. 2017, *AJ*, 153, 2, doi: [10.3847/1538-3881/153/1/2](https://doi.org/10.3847/1538-3881/153/1/2)
- Maguire, K., Eracleous, M., Jonker, P. G., MacLeod, M., & Rosswog, S. 2020, *SSRv*, 216, 39, doi: [10.1007/s11214-020-00661-2](https://doi.org/10.1007/s11214-020-00661-2)
- Martínez-Núñez, S., Kretschmar, P., Bozzo, E., et al. 2017, *SSRv*, 212, 59, doi: [10.1007/s11214-017-0340-1](https://doi.org/10.1007/s11214-017-0340-1)
- Mason, K. O., Breeveld, A., Much, R., et al. 2001, *A&A*, 365, L36, doi: [10.1051/0004-6361:20000044](https://doi.org/10.1051/0004-6361:20000044)
- Matzner, C. D., & McKee, C. F. 1999, *ApJ*, 510, 379, doi: [10.1086/306571](https://doi.org/10.1086/306571)
- McCray, R. 1993, *ARA&A*, 31, 175, doi: [10.1146/annurev.aa.31.090193.001135](https://doi.org/10.1146/annurev.aa.31.090193.001135)
- McMahon, R. G., Banerji, M., Gonzalez, E., et al. 2013, *The Messenger*, 154, 35
- Meegan, C. A., Pendleton, G. N., Briggs, M. S., et al. 1996, *ApJS*, 106, 65, doi: [10.1086/192329](https://doi.org/10.1086/192329)
- Menon, A., & Heger, A. 2017, *MNRAS*, 469, 4649, doi: [10.1093/mnras/stx818](https://doi.org/10.1093/mnras/stx818)
- Menon, A., Utrobin, V., & Heger, A. 2019, *MNRAS*, 482, 438, doi: [10.1093/mnras/sty2647](https://doi.org/10.1093/mnras/sty2647)
- Mereghetti, S., Pons, J. A., & Melatos, A. 2015, *SSRv*, 191, 315, doi: [10.1007/s11214-015-0146-y](https://doi.org/10.1007/s11214-015-0146-y)
- Metcalf, N., Farrow, D. J., Cole, S., et al. 2013, *MNRAS*, 435, 1825, doi: [10.1093/mnras/stt1343](https://doi.org/10.1093/mnras/stt1343)
- Modjaz, M., Li, W., Butler, N., et al. 2009, *ApJ*, 702, 226, doi: [10.1088/0004-637X/702/1/226](https://doi.org/10.1088/0004-637X/702/1/226)
- Morii, M., Tomida, H., Kimura, M., et al. 2013, *ApJ*, 779, 118, doi: [10.1088/0004-637X/779/2/118](https://doi.org/10.1088/0004-637X/779/2/118)
- Mukai, K. 2017, *PASP*, 129, 062001, doi: [10.1088/1538-3873/aa6736](https://doi.org/10.1088/1538-3873/aa6736)
- Müller, B. 2016, *PASA*, 33, e048, doi: [10.1017/pasa.2016.40](https://doi.org/10.1017/pasa.2016.40)
- Nakar, E., & Sari, R. 2010, *ApJ*, 725, 904, doi: [10.1088/0004-637X/725/1/904](https://doi.org/10.1088/0004-637X/725/1/904)
- Nasa High Energy Astrophysics Science Archive Research Center (Heasarc). 2014, HEASoft: Unified Release of FTOOLS and XANADU, Astrophysics Source Code Library. <http://ascl.net/1408.004>
- Ness, J.-U. 2019, arXiv e-prints, arXiv:1909.09711. <https://arxiv.org/abs/1909.09711>
- Nishizawa, A. J., Hsieh, B.-C., Tanaka, M., & Takata, T. 2020, arXiv e-prints, arXiv:2003.01511. <https://arxiv.org/abs/2003.01511>
- Nooraee, N. 2013, *MNRAS*, 428, 205, doi: [10.1093/mnras/sts024](https://doi.org/10.1093/mnras/sts024)
- Novara, G., Esposito, P., Tiengo, A., et al. 2020, arXiv e-prints, arXiv:2004.10665. <https://arxiv.org/abs/2004.10665>
- Ochsenbein, F., Bauer, P., & Marcout, J. 2000, *A&AS*, 143, 23, doi: [10.1051/aas:2000169](https://doi.org/10.1051/aas:2000169)
- Ofek, E. O. 2009, *PASP*, 121, 814, doi: [10.1086/605389](https://doi.org/10.1086/605389)
- Oke, J. B., & Gunn, J. E. 1983, *ApJ*, 266, 713, doi: [10.1086/160817](https://doi.org/10.1086/160817)
- Osten, R. A., Godet, O., Drake, S., et al. 2010, *ApJ*, 721, 785, doi: [10.1088/0004-637X/721/1/785](https://doi.org/10.1088/0004-637X/721/1/785)
- Osten, R. A., Kowalski, A., Drake, S. A., et al. 2016, *ApJ*, 832, 174, doi: [10.3847/0004-637X/832/2/174](https://doi.org/10.3847/0004-637X/832/2/174)
- Pallavicini, R., Tagliaferri, G., & Stella, L. 1990, *A&A*, 228, 403
- Palmer, D. M., Barthelmy, S., Gehrels, N., et al. 2005, *Nature*, 434, 1107, doi: [10.1038/nature03525](https://doi.org/10.1038/nature03525)
- Pandey, J. C., & Singh, K. P. 2008, *MNRAS*, 387, 1627, doi: [10.1111/j.1365-2966.2008.13342.x](https://doi.org/10.1111/j.1365-2966.2008.13342.x)
- Pecaut, M. J., & Mamajek, E. E. 2013, *ApJS*, 208, 9, doi: [10.1088/0067-0049/208/1/9](https://doi.org/10.1088/0067-0049/208/1/9)
- Petrosian, V. 1976, *ApJL*, 210, L53, doi: [10.1086/182301](https://doi.org/10.1086/182301)
- Phinney, E. S. 1989, in *IAU Symposium*, Vol. 136, The Center of the Galaxy, ed. M. Morris (Springer Netherlands), 543
- Piro, A. L., Chang, P., & Weinberg, N. N. 2010, *ApJ*, 708, 598, doi: [10.1088/0004-637X/708/1/598](https://doi.org/10.1088/0004-637X/708/1/598)
- Plucinsky, P. P., Beardmore, A. P., Foster, A., et al. 2017, *A&A*, 597, A35, doi: [10.1051/0004-6361/201628824](https://doi.org/10.1051/0004-6361/201628824)
- Polletta, M., Tajer, M., Maraschi, L., et al. 2007, *ApJ*, 663, 81, doi: [10.1086/518113](https://doi.org/10.1086/518113)
- Predehl, P. 2017, *Astronomische Nachrichten*, 338, 159, doi: [10.1002/asna.201713324](https://doi.org/10.1002/asna.201713324)
- Predehl, P., & Schmitt, J. H. M. M. 1995, *A&A*, 500, 459
- Predehl, P., Andritschke, R., Böhringer, H., et al. 2010, in *Society of Photo-Optical Instrumentation Engineers (SPIE) Conference Series*, Vol. 7732, Proc. SPIE, 77320U, doi: [10.1117/12.856577](https://doi.org/10.1117/12.856577)
- Pye, J. P., Rosen, S., Fyfe, D., & Schröder, A. C. 2015, *A&A*, 581, A28, doi: [10.1051/0004-6361/201526217](https://doi.org/10.1051/0004-6361/201526217)

- Racusin, J. L., Liang, E. W., Burrows, D. N., et al. 2009, *ApJ*, 698, 43, doi: [10.1088/0004-637X/698/1/43](https://doi.org/10.1088/0004-637X/698/1/43)
- Rees, M. J. 1988, *Nature*, 333, 523, doi: [10.1038/333523a0](https://doi.org/10.1038/333523a0)
- Robrade, J., Poppenhaeger, K., & Schmitt, J. H. M. M. 2010, *A&A*, 513, A12, doi: [10.1051/0004-6361/200913603](https://doi.org/10.1051/0004-6361/200913603)
- Robrade, J., & Schmitt, J. H. M. M. 2005, *A&A*, 435, 1073, doi: [10.1051/0004-6361:20041941](https://doi.org/10.1051/0004-6361:20041941)
- Romano, P. 2015, *Journal of High Energy Astrophysics*, 7, 126, doi: [10.1016/j.jheap.2015.04.008](https://doi.org/10.1016/j.jheap.2015.04.008)
- Rosen, S. R., Webb, N. A., Watson, M. G., et al. 2016, *A&A*, 590, A1, doi: [10.1051/0004-6361/201526416](https://doi.org/10.1051/0004-6361/201526416)
- Sapir, N., & Halbertal, D. 2014, *ApJ*, 796, 145, doi: [10.1088/0004-637X/796/2/145](https://doi.org/10.1088/0004-637X/796/2/145)
- Sapir, N., Katz, B., & Waxman, E. 2011, *ApJ*, 742, 36, doi: [10.1088/0004-637X/742/1/36](https://doi.org/10.1088/0004-637X/742/1/36)
- . 2013, *The Astrophysical Journal*, 774, 79, doi: [10.1088/0004-637X/774/1/79](https://doi.org/10.1088/0004-637X/774/1/79)
- Sartore, N., Ripamonti, E., Treves, A., & Turolla, R. 2010, *A&A*, 510, A23, doi: [10.1051/0004-6361/200912222](https://doi.org/10.1051/0004-6361/200912222)
- Schwarz, G. J., Ness, J.-U., Osborne, J. P., et al. 2011, *ApJS*, 197, 31, doi: [10.1088/0067-0049/197/2/31](https://doi.org/10.1088/0067-0049/197/2/31)
- Sguera, V., Sidoli, L., Bird, A. J., Paizis, A., & Bazzano, A. 2020, *MNRAS*, 491, 4543, doi: [10.1093/mnras/stz3330](https://doi.org/10.1093/mnras/stz3330)
- Shen, R.-F. 2019, *ApJL*, 871, L17, doi: [10.3847/2041-8213/aafc64](https://doi.org/10.3847/2041-8213/aafc64)
- Shen, S., Mo, H. J., White, S. D. M., et al. 2003, *MNRAS*, 343, 978, doi: [10.1046/j.1365-8711.2003.06740.x](https://doi.org/10.1046/j.1365-8711.2003.06740.x)
- Skrutskie, M. F., Cutri, R. M., Stiening, R., et al. 2006, *AJ*, 131, 1163, doi: [10.1086/498708](https://doi.org/10.1086/498708)
- Smartt, S. J. 2009, *ARA&A*, 47, 63, doi: [10.1146/annurev-astro-082708-101737](https://doi.org/10.1146/annurev-astro-082708-101737)
- Soderberg, A. M., Berger, E., Page, K. L., et al. 2008, *Nature*, 453, 469, doi: [10.1038/nature06997](https://doi.org/10.1038/nature06997)
- Starrfield, S., Iliadis, C., & Hix, W. R. 2016, *PASP*, 128, 051001, doi: [10.1088/1538-3873/128/963/051001](https://doi.org/10.1088/1538-3873/128/963/051001)
- Strüder, L., Briel, U., Dennerl, K., et al. 2001, *A&A*, 365, L18, doi: [10.1051/0004-6361:20000066](https://doi.org/10.1051/0004-6361:20000066)
- Sun, H., Li, Y., Zhang, B.-B., et al. 2019, *ApJ*, 886, 129, doi: [10.3847/1538-4357/ab4bc7](https://doi.org/10.3847/1538-4357/ab4bc7)
- Suzuki, A., & Shigeyama, T. 2010, *ApJL*, 717, L154, doi: [10.1088/2041-8205/717/2/L154](https://doi.org/10.1088/2041-8205/717/2/L154)
- . 2013, *ApJL*, 764, L12, doi: [10.1088/2041-8205/764/1/L12](https://doi.org/10.1088/2041-8205/764/1/L12)
- Svirski, G., & Nakar, E. 2014, *ApJ*, 788, 113, doi: [10.1088/0004-637X/788/2/113](https://doi.org/10.1088/0004-637X/788/2/113)
- Tachibana, Y., & Miller, A. A. 2018, *PASP*, 130, 128001, doi: [10.1088/1538-3873/aae3d9](https://doi.org/10.1088/1538-3873/aae3d9)
- Taddia, F., Sollerman, J., Fremling, C., et al. 2019, *A&A*, 621, A71, doi: [10.1051/0004-6361/201834429](https://doi.org/10.1051/0004-6361/201834429)
- Turner, M. J. L., Abbey, A., Arnaud, M., et al. 2001, *A&A*, 365, L27, doi: [10.1051/0004-6361:20000087](https://doi.org/10.1051/0004-6361:20000087)
- Turolla, R., Zane, S., & Watts, A. L. 2015, *Reports on Progress in Physics*, 78, 116901, doi: [10.1088/0034-4885/78/11/116901](https://doi.org/10.1088/0034-4885/78/11/116901)
- Utrobin, V. P., Wongwathanarat, A., Janka, H.-T., et al. 2019, *A&A*, 624, A116, doi: [10.1051/0004-6361/201834976](https://doi.org/10.1051/0004-6361/201834976)
- van den Eijnden, J., Bagnoli, T., Degenaar, N., et al. 2017, *MNRAS*, 466, L98, doi: [10.1093/mnrasl/slw244](https://doi.org/10.1093/mnrasl/slw244)
- van der Walt, S., Colbert, S. C., & Varoquaux, G. 2011, *Computing in Science Engineering*, 13, 22, doi: [10.1109/MCSE.2011.37](https://doi.org/10.1109/MCSE.2011.37)
- Verner, D. A., & Yakovlev, D. G. 1995, *A&AS*, 109, 125
- Vikhlinin, A. 1998, *The Astrophysical Journal*, 505, L123, doi: [10.1086/311606](https://doi.org/10.1086/311606)
- Villasenor, J. S., Lamb, D. Q., Ricker, G. R., et al. 2005, *Nature*, 437, 855, doi: [10.1038/nature04213](https://doi.org/10.1038/nature04213)
- Virtanen, P., Gommers, R., Oliphant, T. E., et al. 2020, *Nature Methods*, 17, 261, doi: [10.1038/s41592-019-0686-2](https://doi.org/10.1038/s41592-019-0686-2)
- von Kienlin, A., Meegan, C. A., Paciesas, W. S., et al. 2020, *ApJ*, 893, 46, doi: [10.3847/1538-4357/ab7a18](https://doi.org/10.3847/1538-4357/ab7a18)
- Walter, R., Lutovinov, A. A., Bozzo, E., & Tsygankov, S. S. 2015, *A&A Rv*, 23, 2, doi: [10.1007/s00159-015-0082-6](https://doi.org/10.1007/s00159-015-0082-6)
- Watson, M. G., Schröder, A. C., Fyfe, D., et al. 2009, *A&A*, 493, 339, doi: [10.1051/0004-6361:200810534](https://doi.org/10.1051/0004-6361:200810534)
- Waxman, E., & Katz, B. 2017, *Shock Breakout Theory* (Springer International Publishing AG), 967, doi: [10.1007/978-3-319-21846-5\\_33](https://doi.org/10.1007/978-3-319-21846-5_33)
- Weaver, T. A. 1976, *ApJS*, 32, 233, doi: [10.1086/190398](https://doi.org/10.1086/190398)
- Wenger, M., Ochsenbein, F., Egret, D., et al. 2000, *A&AS*, 143, 9, doi: [10.1051/aas:2000332](https://doi.org/10.1051/aas:2000332)
- Williams, P. K. G., Cook, B. A., & Berger, E. 2014, *ApJ*, 785, 9, doi: [10.1088/0004-637X/785/1/9](https://doi.org/10.1088/0004-637X/785/1/9)
- Willingale, R., Starling, R. L. C., Beardmore, A. P., Tanvir, N. R., & O'Brien, P. T. 2013, *MNRAS*, 431, 394, doi: [10.1093/mnras/stt175](https://doi.org/10.1093/mnras/stt175)
- Wilms, J., Allen, A., & McCray, R. 2000, *ApJ*, 542, 914, doi: [10.1086/317016](https://doi.org/10.1086/317016)
- Wolf, C., Meisenheimer, K., Rix, H. W., et al. 2003, *A&A*, 401, 73, doi: [10.1051/0004-6361:20021513](https://doi.org/10.1051/0004-6361:20021513)
- Wolf, C., Onken, C. A., Luvaul, L. C., et al. 2018, *PASA*, 35, e010, doi: [10.1017/pasa.2018.5](https://doi.org/10.1017/pasa.2018.5)
- Wongwathanarat, A., Müller, E., & Janka, H.-T. 2015, *A&A*, 577, A48, doi: [10.1051/0004-6361/201425025](https://doi.org/10.1051/0004-6361/201425025)
- Woosley, S. E., Pinto, P. A., Martin, P. G., & Weaver, T. A. 1987, *ApJ*, 318, 664, doi: [10.1086/165402](https://doi.org/10.1086/165402)
- Wright, A. H., Hildebrandt, H., Kuijken, K., et al. 2019, *A&A*, 632, A34, doi: [10.1051/0004-6361/201834879](https://doi.org/10.1051/0004-6361/201834879)

- Xue, Y. Q., Zheng, X. C., Li, Y., et al. 2019, *Nature*, 568, 198, doi: [10.1038/s41586-019-1079-5](https://doi.org/10.1038/s41586-019-1079-5)
- Yang, G., Brandt, W. N., Zhu, S. F., et al. 2019, *Monthly Notices of the Royal Astronomical Society*, 487, 4721, doi: [10.1093/mnras/stz1605](https://doi.org/10.1093/mnras/stz1605)
- Yaqoob, T. 1998, *ApJ*, 500, 893, doi: [10.1086/305781](https://doi.org/10.1086/305781)
- York, D. G., Adelman, J., Anderson, John E., J., et al. 2000, *AJ*, 120, 1579, doi: [10.1086/301513](https://doi.org/10.1086/301513)
- Zhang, B.-B., Liang, E.-W., & Zhang, B. 2007, *ApJ*, 666, 1002, doi: [10.1086/519548](https://doi.org/10.1086/519548)